Atmos. Chem. Phys., 15, 13217–13239, 2015
www.atmos-chem-phys.net/15/13217/2015/
doi:10.5194/acp-15-13217-2015
© Author(s) 2015. CC Attribution 3.0 License.

Atmospheric Chemistry and Physics
Open Access
EGU

# LSA SAF Meteosat FRP products – Part 1: Algorithms, product contents, and analysis

**M. J. Wooster**[1,2], **G. Roberts**[3], **P. H. Freeborn**[1,4], **W. Xu**[1], **Y. Govaerts**[5], **R. Beeby**[1], **J. He**[1], **A. Lattanzio**[6], **D. Fisher**[1,2], **and R. Mullen**[1]

[1]King's College London, Environmental Monitoring and Modelling Research Group, Department of Geography , Strand, London, WC2R 2LS, UK
[2]NERC National Centre for Earth Observation (NCEO), UK
[3]Geography and Environment, University of Southampton, Highfield, Southampton SO17 1BJ, UK
[4]Fire Sciences Laboratory, Rocky Mountain Research Station, US Forest Service, Missoula, Montana, USA
[5]Rayference, Brussels, Belgium
[6]MakaluMedia, Darmstadt, Germany

*Correspondence to:* G. Roberts (g.j.roberts@soton.ac.uk)

Received: 31 December 2014 – Published in Atmos. Chem. Phys. Discuss.: 12 June 2015
Revised: 23 October 2015 – Accepted: 11 November 2015 – Published: 30 November 2015

**Abstract.** Characterizing changes in landscape fire activity at better than hourly temporal resolution is achievable using thermal observations of actively burning fires made from geostationary Earth Observation (EO) satellites. Over the last decade or more, a series of research and/or operational "active fire" products have been developed from geostationary EO data, often with the aim of supporting biomass burning fuel consumption and trace gas and aerosol emission calculations. Such Fire Radiative Power (FRP) products are generated operationally from Meteosat by the Land Surface Analysis Satellite Applications Facility (LSA SAF) and are available freely every 15 min in both near-real-time and archived form. These products map the location of actively burning fires and characterize their rates of thermal radiative energy release (FRP), which is believed proportional to rates of biomass consumption and smoke emission. The FRP-PIXEL product contains the full spatio-temporal resolution FRP data set derivable from the SEVIRI (Spinning Enhanced Visible and Infrared Imager) imager onboard Meteosat at a 3 km spatial sampling distance (decreasing away from the west African sub-satellite point), whilst the FRP-GRID product is an hourly summary at 5° grid resolution that includes simple bias adjustments for meteorological cloud cover and regional underestimation of FRP caused primarily by under-detection of low FRP fires. Here we describe the enhanced geostationary Fire Thermal Anomaly (FTA) detection algorithm used to deliver these products and detail the methods used to generate the atmospherically corrected FRP and per-pixel uncertainty metrics. Using SEVIRI scene simulations and real SEVIRI data, including from a period of Meteosat-8 "special operations", we describe certain sensor and data pre-processing characteristics that influence SEVIRI's active fire detection and FRP measurement capability, and use these to specify parameters in the FTA algorithm and to make recommendations for the forthcoming Meteosat Third Generation operations in relation to active fire measures. We show that the current SEVIRI FTA algorithm is able to discriminate actively burning fires covering down to $10^{-4}$ of a pixel and that it appears more sensitive to fire than other algorithms used to generate many widely exploited active fire products. Finally, we briefly illustrate the information contained within the current Meteosat FRP-PIXEL and FRP-GRID products, providing example analyses for both individual fires and multi-year regional-scale fire activity; the companion paper (Roberts et al., 2015) provides a full product performance evaluation and a demonstration of product use within components of the Copernicus Atmosphere Monitoring Service (CAMS).

## 1 Introduction

### 1.1 Meteosat Second Generation and biomass burning observations

Smoke emissions from landscape-scale fires are strong influencers of atmospheric composition, chemistry, and climate (Williams et al., 2010), and Earth Observation (EO) satellites are key to their characterization. The European Organisation for the Exploitation of Meteorological Satellites (EUMETSAT) currently operates the Meteosat Second Generation (MSG) system, Europe's geostationary EO programme for studying weather, climate, and Earth's environment. Meteosat carries the Spinning Enhanced Visible and Infrared Imager (SEVIRI), whose data can be used to detect actively burning fires and to estimate their Fire Radiative Power (FRP). FRP has been shown in laboratory and field experiments to be proportional to rates of fuel consumption and smoke production (Wooster et al., 2005; Freeborn et al., 2008; Kremens et al., 2012; Pereira et al., 2011). Since the first MSG launch in 2002, SEVIRI has observed Europe, Africa, and parts of South America every 15 min, and provided the first geostationary EO data to be used to estimate FRP from landscape fires (Roberts et al., 2005; Wooster et al., 2005; Roberts and Wooster, 2008; Roberts et al., 2009a, b). SEVIRI-derived FRP data have been used to paremeterize high temporal resolution smoke emissions fields for atmospheric modelling (Baldassarre et al., 2015), including within the Copernicus Atmosphere Monitoring Service (CAMS; Roberts et al., 2015). Here we describe the algorithms and characteristics of the SEVIRI FRP products available operationally from the EUMETSAT Land Surface Analysis Satellite Applications Facility (LSA SAF; http://landsaf.ipma.pt). These products are available via both near-real time and offline dissemination routes and have already provided information used in a number of biomass burning emissions inventories (e.g. Turquety et al., 2014) and to the Global Fire Assimilation System (GFAS) that provides fire emissions data to the CAMS (e.g. Hollingsworth et al., 2008; Kaiser et al., 2012; Andela et al., 2015).

### 1.2 Landscape-scale fires and smoke emissions

Including a sufficiently accurate spatio-temporal description of landscape fire emissions is a fundamental pre-requisite for certain atmospheric "information services", including those aimed at studying long-range transport of air pollutants (Reid et al., 2009), the near-real-time monitoring and forecasting of air quality (e.g. Sofiev et al., 2009; Kaiser et al., 2012), and the determination of atmospheric composition variations (Clerbaux et al., 2009; Ross et al., 2013). Furthermore, carbon accounting parameters derived from EO-derived FRP data are contributing to long-term regional and global biomass burning emissions inventories (e.g. Remy and Kaiser, 2014; Roberts et al., 2011; Vermote et al., 2009; Zhang et al., 2012), which in turn can be used to gauge compliance with international treaties on greenhouse gas (GHG) and air pollutant emission ceilings. In this context, the type of very high temporal resolution active fire information available operationally in near-real time from SEVIRI (Fig. 1a) are very complementary to the higher spatial resolution, but more temporally limited, views of the same fires available from polar orbiters (Fig. 1b) (e.g. Giglio et al., 2003; Wooster et al., 2012; Schroeder et al., 2014). A high temporal resolution view is particularly useful because fires generally show substantial short-term activity variations and radical diurnal shifts in behaviour (Roberts et al., 2009a; Andela et al., 2015). Rapidly supplied, regularly updated active fire information can even provide useful information for early warning and near-continuous tracking of new fire activity (e.g. Dlamini, 2009).

Using an operational version of the geostationary Fire Thermal Anomaly (FTA) algorithm of Roberts and Wooster (2008), the MSG satellites provide high temporal resolution FRP data relating to fires burning across the African and European continents and also the eastern edge of South America (see Fig. S1 in the Supplement for the Meteosat disk). Africa is considered the most "fire-affected" continent, responsible for $\sim$ 30–50 % of the global burned area and a very significant proportion of annual global fire emissions (Andreae, 1991; van der Werf et al., 2003, 2006). Landscape burning is also relatively common across parts of Europe and, occasionally, extreme "wildfire" outbreaks can threaten large population centres and/or deliver acute air quality impacts, particularly in southern Europe (Liu et al., 2009; Baldassarre et al., 2015; Roberts et al., 2015). The region of South America viewed by SEVIRI is primarily dry and moist forest, cerrado and croplands, which is also greatly affected by fires; however, because of the extreme SEVIRI view angles, the FTA algorithm applied to the GOES (Geostationary Operational Environmental Satellites) imager provides better geostationary FRP data here (Xu et al., 2010).

### 1.3 LSA SAF Meteosat SEVIRI FRP products

Two Meteosat SEVIRI FRP products are delivered operationally in near-real time and archived form by the EUMETSAT LSA SAF (http://landsaf.ipma.pt), whose mission is described in Trigo et al. (2011). These are the Level 2 FRP-PIXEL product, delivered at SEVIRI's full spatial and temporal resolution, and the Level 3 spatio-temporal summary FRP-GRID product. Here we document the algorithms and information content relevant to both products, focusing in particular on enhancements made to the prototype FTA algorithm first described in Roberts and Wooster (2008) and also to the retrieval of FRP and its associated uncertainties. We illustrate how the SEVIRI pre-processing chain influences these retrievals, and demonstrate differences between the FRP-PIXEL and an alternative active fire product (WF-ABBA-SEVIRI) also being generated from SEVIRI

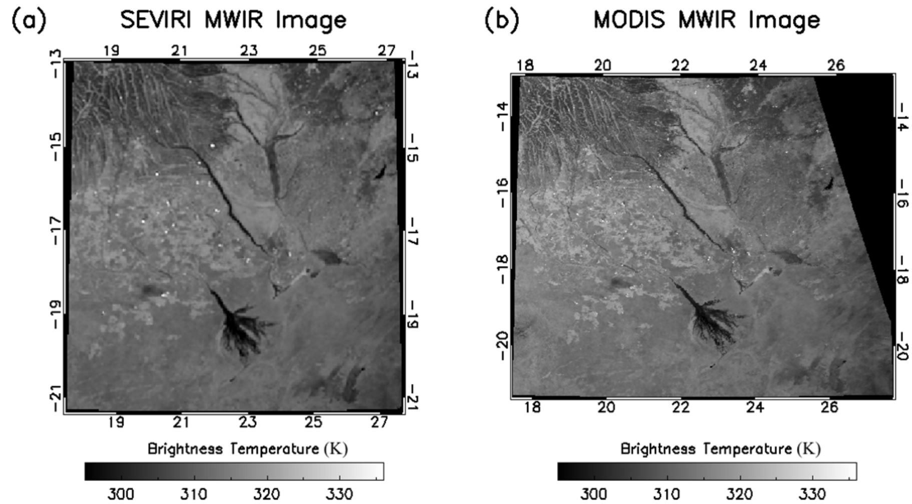


**Figure 1.** Near-simultaneous MWIR channel imagery of fires in southern Africa from **(a)** SEVIRI (IR3.9) and **(b)** MODIS (Band 21). These image subsets show pixels with elevated MWIR brightness temperatures as bright, almost all of these are likely caused by actively burning fires. The area shown includes the Okavango Delta wetland (around 250 km long), which shows up as relatively cooler than the surrounding dry land. The SEVIRI data were collected at 12:50 UTC on 17 August 2007 and the MODIS data around 10 min earlier. The polar orbiting MODIS and geostationary SEVIRI data are not exactly co-registered but cover approximately the same area. Whilst the increased spatial resolution of the MODIS data is clear and allows more fires to be visually identified via their elevated MWIR signals, many of the fires can also clearly be seen in the SEVIRI imagery (albeit with lower MWIR brightness temperatures since the fires are filling a lower proportion of the larger SEVIRI pixel than the matching MODIS pixels). SEVIRI provides 96 images per day (one every 15 min) at a consistent view zenith angle. At this latitude, MODIS provides up to four images per day, though some of these will be at extreme view zenith angles of up to 65° under which conditions the MODIS spatial fidelity is far reduced, with each pixel covering approximately the same ground area as a SEVIRI pixel (Freeborn et al., 2011). The local afternoon imaging time of MODIS Aqua, as used here, is also relatively close to the typical peak of the fire diurnal cycle (Roberts et al., 2009a), but the times of the other MODIS overpasses are significantly distant from this.

observations. The companion paper (Roberts et al., 2015) provides detailed product performance evaluation, a much more extensive SEVIRI fire product intercomparison, and a demonstration of use of the FRP-PIXEL product in the characterization of fire emissions within CAMS. Finally, we provide recommendations for pre-processing considerations related to Meteosat Third Generation observations of active fires.

## 2 Overview of the LSA SAF FRP product generation

### 2.1 Active fire data from the MSG satellite series

There are a total of four spin-stabilized MSG satellites in orbit (Meteosat-8–11), launched in 2002, 2005, 2012, and 2015 respectively. Each rotates at a speed of 100 rpm and provides Earth images from the SEVIRI spin scan radiometer (Aminou et al., 1997; Aminou, 2002). The primary full Earth disk MSG observatory is located at 0° longitude, whilst the others provide rapid scanning services over a reduced fraction of the Earth disk and/or backup capabilities.

SEVIRI operates in 12 spectral channels (Aminou et al., 1997), and the fact that the midwave infrared (MWIR: IR3.9) and longwave infrared (LWIR: IR10.8 and IR12.0) bands (Channels 4, 9, and 10 in Table 1) are differently sensitive to the thermal radiance emitted by high temperature sources (e.g. Prins et al., 1998) allows SEVIRI in theory to detect actively burning fires covering as little as $10^{-4}$ of a pixel (Roberts et al., 2005; Wooster et al., 2013). However, the FTA algorithm must take care to prevent sunglint and other potentially confounding features being falsely identified as active fires, and this requires use of data from other SEVIRI spectral channels (Sect. 3). Confirmed active fire pixels have their FRP estimated using the MIR (mid-infrared) radiance method of Wooster et al. (2003, 2005; Sect. 4), with delivery of a full per-pixel FRP uncertainty measure provided using methods outlined in Sect. 5.

### 2.2 SEVIRI data capture and pre-processing

As the Meteosat satellite spins (east-to-west), SEVIRI's scan mirror is stepped (south-to-north) to build up an image of the full Earth disk over a period of $\sim$12.5 min (Aminou, 2002). The full repeat cycle is $\sim$15 min, though shorter if only part of the Earth disk is imaged. SEVIRI's diamond-shaped pixels have an instantaneous field of view (IFOV) of 4.8 km × 4.8 km at the west African sub-satellite point (SSP), with an SSP ground sampling distance of 3 km (full width at half maximum, FWHM) and a final image resolution of around 6 km (Just, 2000; Aminou, 2002; Schmetz et

**Table 1.** Spectral bands of Meteosat SEVIRI.

| Channel No. | Spectral band (µm) | Band characteristics (wavelength, µm) Centre | Min. | Max. | Main observational applications |
|---|---|---|---|---|---|
| 1 | VIS0.6 | 0.635 | 0.56 | 0.71 | Surface, clouds, wind fields |
| 2 | VIS0.8 | 0.81 | 0.74 | 0.88 | Surface, clouds, wind fields |
| 3 | NIR1.6 | 1.64 | 1.50 | 1.78 | Surface, cloud phase |
| 4 | IR3.9 | 3.90 | 3.48 | 4.36 | Surface, clouds, wind fields |
| 5 | WV6.2 | 6.25 | 5.35 | 7.15 | Water vapour, high level clouds, atmospheric instability |
| 6 | WV7.3 | 7.35 | 6.85 | 7.85 | Water vapour, atmospheric instability |
| 7 | IR8.7 | 8.70 | 8.30 | 9.1 | Surface, clouds, atmospheric instability |
| 8 | IR9.7 | 9.66 | 9.38 | 9.94 | Ozone |
| 9 | IR10.8 | 10.80 | 9.80 | 11.80 | Surface, clouds, wind fields, atmospheric instability |
| 10 | IR12.0 | 12.00 | 11.00 | 13.00 | Surface, clouds, atmospheric instability |
| 11 | IR13.4 | 13.40 | 12.40 | 14.40 | Cirrus cloud height, atmospheric instability |
| 12 | HRV | Broadband (about 0.4–1.1 µm) | Surface, clouds | | |

al., 2002; Calle et al., 2009). These distances increase with view zenith angle, yielding larger and more widely separated ground footprints further from the SSP.

SEVIRI data are transmitted from the MSG satellites to the primary ground station (PGS) in Usingen (Germany), and then sent to the image processing facility (IMPF) at Darmstadt (Just, 2000; Murphy, 2013) to be radiometrically/geometrically corrected and geolocated from level 1.0 to level 1.5. They are then forwarded to users, including the LSA SAF headquartered at the Instituto Portugues do Mar e da Atmosfera in Portugal (DaCamara, 2006; Trigo et al., 2011).

## 2.3 Introduction to the LSA SAF Meteosat SEVIRI FRP product suite

As with all other current Level 2 LSA SAF products (Trigo et al., 2011) the FRP-PIXEL product is currently generated separately for the four geographic regions of the Meteosat disk: Europe (Euro), Northern Africa (NAfr), Southern Africa (SAfr), and South America (SAme) (see Fig. S1), though this split dissemination will soon be replaced by the delivery of full disk Level 2 products. The Level 3 FRP-GRID product is already full disk, albeit at a reduced spatio-temporal resolution, and includes simple adjustments for cloud cover and for SEVIRI's inability to detect the lowest FRP fires (Freeborn et al., 2009),

Each FRP-PIXEL product actually consists of two separate product files: (i) an FRP-PIXEL List Product file that stores variables derived at each detected active fire pixel, and (ii) an FRP-PIXEL Quality Product file that contains a 2-D array of flags recording the processing status of each SEVIRI pixel, not just those identified as containing active fires (e.g. whether the FTA algorithm classified a pixel as water, cloud-contaminated, sun glint-affected, cloud-free but with no fires, or as a confirmed "true" active fire pixel). The Quality Product codes are shown in Table S1 of the Supplement, which also includes further details on product structure and accessibility (as in http://landsaf.ipma.pt).

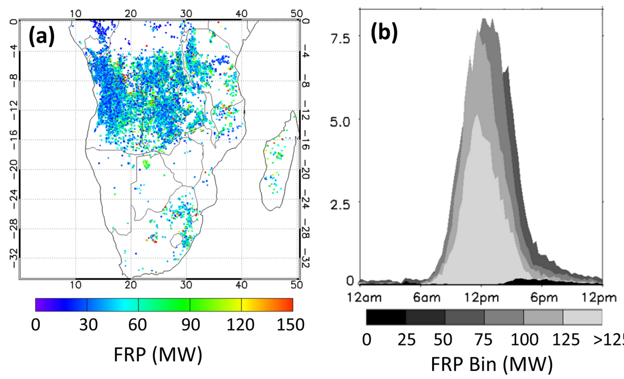


**Figure 2.** Example data extracted from the LSA SAF Meteosat SEVIRI FRP-PIXEL product. **(a)** Active fire locations and their FRP as measured on 17 July 2009 over southern Africa. **(b)** The same data but now shown as the diurnal cycle of FRP binned into 25 MW increments. These data indicate that the individual fire pixel FRP values recorded on this date almost all lay below 150 MW and that the peak of the diurnal cycle generally occurred earlier in the day for higher FRP fire pixels.

Because the FRP-PIXEL product files are able to be delivered to users within 1 h of image acquisition and are thus more frequent and more timely than most other EO active fire products, they can capture the high frequency FRP fluctuations shown by landscape-scale fires and may meet some of the demands for "rapid response/decision support" fire products (Frost and Annegarn, 2007). Figure 2 illustrates one example of the spatio-temporal distribution of active fire data extracted from the 96 FRP-PIXEL List Product files covering Southern Africa during a single day. Freeborn et al. (2014a) recently demonstrated that, over regions of central Africa,

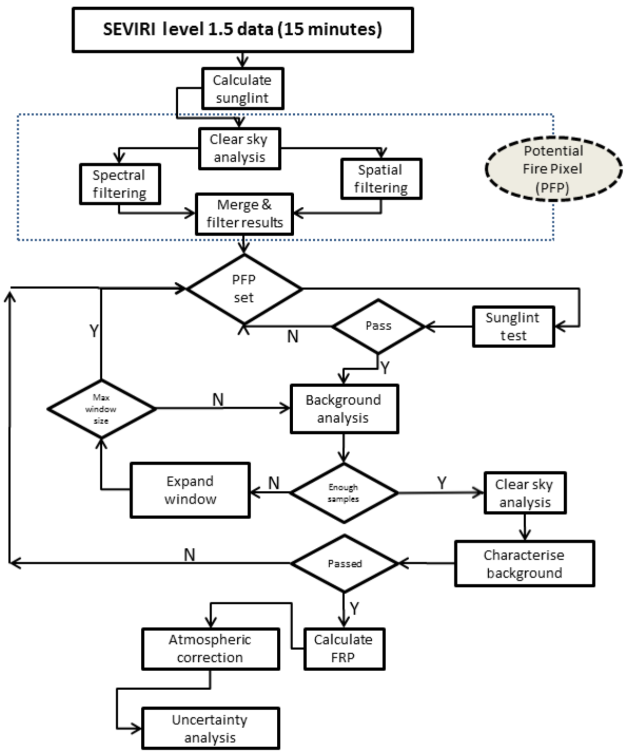


**Figure 3.** Flowchart illustrating the FRP-PIXEL product processing chain, which uses the operational geostationary FTA algorithm described herein. The processing chain acts upon the input level 1.5 data from each SEVIRI imaging slot independently, and the procedures outlined by the blue dotted box are those involved in the selection of the potential fire pixels (PFPs). These PFPs are then subject to a series of thresholding procedures, based on spatially varying "contextual" thresholds, used to determine whether or not each FPF can be confirmed as a true active fire pixel and have its FRP assessed.

the FTA algorithm successfully detects fire pixels having an FRP down to around 10 MW. However, below around 30–40 MW active fire pixel counts are increasingly underestimated due to the difficulty in detecting these lower FRP fire pixels within the relatively coarse SEVIRI pixels, and Fig. 2 indicates very low numbers of fire pixels with a FRP of less than 25 MW are detected on this day. Adjustments are applied in the FRP-GRID product to account for this effect and thus better estimate landscape-scale regional FRP totals (Sect. 6).

## 3 Operational implementation of the geostationary (FTA) algorithm

### 3.1 The FRP-PIXEL product processing chain

The LSA SAF FRP product processing chain (Fig. 3) ingests level 1.5 SEVIRI data (calibrated into $\mathrm{mW\,m^{-2}\,sr^{-1}\,(cm^{-1})^{-1}}$ and into K for the infrared channels). The online Algorithm Theoretical Basis Document (ATBD) available at http://landsaf.ipma.pt provides full details, whereas we provide here the key features and operational enhancements made beyond the Roberts and Wooster (2008) FTA algorithm prototype.

### 3.2 Pre-processing stage: water, cloud, and smoke discrimination

Sunglint from water can result in false active fire detections (Zhukov et al., 2006), so SEVIRI pixels containing major water bodies are masked using the 1 km Global Land Cover (GLC 2000) map of Mayaux et al. (2004). Clouds can cause similar problems and may also contaminate the background window characteristics used in the "contextual" active fire pixel confirmation stage (Sect. 3.5), but smoke need not be masked since active fires often remain highly detectable through smoke (Libonati et al., 2010). LSA SAF processing currently uses the Nowcasting and Very Short Range Forecasting SAF (NWC SAF; www.nwcsaf.org) cloud mask (CMa; Derrien and Le Gleau, 2005), with CMa pixels reclassed as non-cloudy for the fire application if their cloudy classification is based on either of the following tests, which are fully detailed in Derrien and Le Gleau (2005) and MeteoFrance (2010).

i. The local spatial texture test, applied to a 3×3 pixel window to detect broken clouds/cloud edges by exploiting the higher spatial variations typical of visible (0.6 µm), NIR (0.8 µm) and/or LWIR channel measures around such features. Areas of active fire and smoke often show similar spatial variations, so the test is inappropriate here.

ii. The brightness temperature difference (BTD; $\mathrm{BT}_{3.9} - \mathrm{BT}_{10.8}$) test, which detects semi-transparent clouds at night and low-level clouds during the day, exploiting the lower water cloud emissivity in the SEVIRI IR3.9 channel as compared to the IR10.8 channel. BTD increases over active fires, so a CMa BTD-classified pixel only remains cloudy if it passes the following three conditions:

$$\mathrm{BT}_{3.9} - \mathrm{BT}_{10.8} > 6.0\,\mathrm{K}, \tag{1}$$

$$\mathrm{BT}_{10.8} - \mathrm{BT}_{12.0} > 1.5\,\mathrm{K}, \tag{2}$$

$$\frac{L_{3.9}}{L_{0.64}} < 0.7\,, \tag{3}$$

where $\mathrm{BT}_{3.9}$, $\mathrm{BT}_{10.8}$, and $\mathrm{BT}_{12.0}$ are the pixel brightness temperatures in the SEVIRI IR3.9 (MWIR), IR10.8 µm (LWIR) and IR12.0 µm (LWIR) channels, respectively, and $L_{3.9}$ and $L_{0.64}$ are the spectral radiances in the IR3.9 and VIS0.6 µm (visible) channels, respectively (see Table 1).

iii. The spatial smoothing test, which fills in cloud detection "gaps" in areas of semi-transparent cloud. If at least

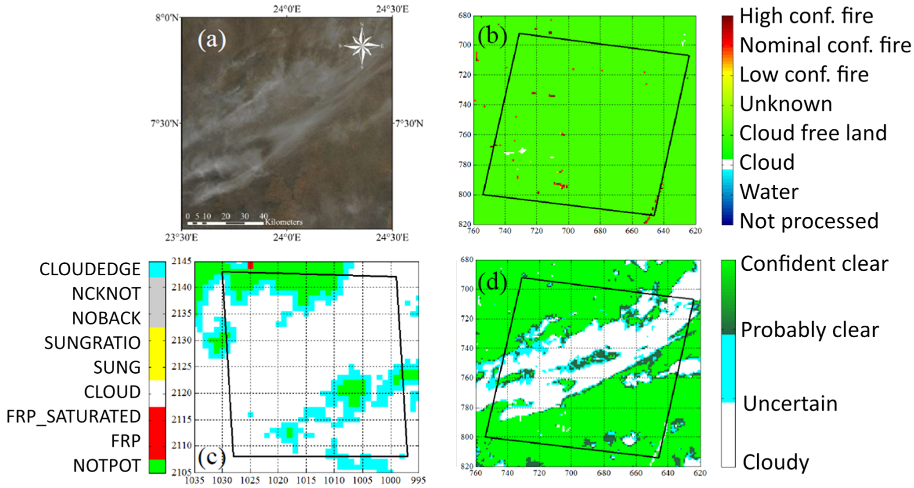


**Figure 4.** Simultaneous data collected by the Aqua MODIS and Meteosat SEVIRI instruments over a $1^\circ \times 1^\circ$ region of the Central African Republic (CAR) at 12:00 UTC on 11 January 2009. **(a)** 500 m spatial resolution MODIS Aqua true colour composite, **(b)** MODIS fire mask retrieved from the coincident MYD14 active fire and thermal anomaly product, **(c)** the status flags (Table S1) retrieved from the coincident SEVIRI FRP-PIXEL quality file, and **(d)** the MODIS cloud mask retrieved from the coincident MYD35 MODIS cloud product. The MODIS true colour composite image has been reprojected into geographic coordinates and this area is shown boxed on the other products (shown in their native image coordinate systems). It is apparent that the geographically widespread, but somewhat transparent, cloud shown in the MODIS colour composite in **(a)** is widely detected by the MODIS MYD35 cloud mask **(d)** and by the adapted CMa used in the FRP-PIXEL products **(c)**. However, the MODIS cloud mask used in the MODIS fire product **(b)** is specified such that it does not detect such thin clouds and allows fires burning underneath to remain detectable. Far less cloud can be seen to be detected by this mask than by either of the other two masks. The figure is adapted from Freeborn et al. (2014a), who go on to confirm the very strong sensitivity of the SEVIRI CMa of Derrien and Le Gleau (2005) to cloud, compared to that of the MODIS active fire product cloud mask.

three pixels immediately surrounding a cloudy pixel are classed as cloudy based on this test, then the pixel is reclassified as non-cloudy.

CMa pixels remaining after the above adjustments are assigned Class 3 (“cloud”) in the FRP-PIXEL Quality Product (Table S1 in the Supplement). As an indication of the importance of our CMa cloud mask adaptations, 1 day of SEVIRI data of Southern Africa (7 July 2004) was processed using both the standard and adjusted CMas, and was found to show 22 % fewer “confirmed” active fire pixels in the former case. However, despite the adjusted CMa mask being far better suited to FRP product cloud screening, Freeborn et al. (2014a) demonstrate that its performance substantially differs from that of the simpler masks used, for example, within the MODIS (Moderate Resolution Imaging Spectroradiometer) MOD14/MYD14 active fire and thermal anomaly products (Giglio et al., 2003). For example, whilst the adjusted SEVIRI CMa masks thinly and partially cloud-covered pixels, the MOD14/MYD14 product often allows for fire detection in such areas (Fig. 4), albeit the retrieved FRP values maybe perturbed. To assess the potential for the retrieval of FRP values under thinly and/or partially cloud-covered SEVIRI pixels, an analysis was made using an additional “cloud-type” mask where cloudy pixels are further classified according to their optical characteristics obtained from the NWC SAF cloud-type product (CT; Derrien and Le Gleau, 2005). For this analysis, 5 days of SEVIRI data over Southern Africa were processed using the FTA algorithm and potential active fire pixels split into two classes: in clear sky or under optically thin cloud cover (overlying CT mask values of 15, 16, 17, or 19). Following the standard processing of the potential active fire pixels, as shown in Fig. 3, it was found that only $\sim 0.01$ % of those under the optically thin cloud cover were finally classed as confirmed fire pixels. This was initially assumed to be due to the sunglint screening employed by the FTA algorithm, since cloud-contaminated pixels typically exhibit increased radiances in visible channels, leading to their rejection in the middle infrared to red wavelength spectral radiance ratio test (Sect. 3.4). However, when the sunglint screening tests were removed, similar results were obtained with almost all potential active fire pixels being instead rejected at the background characterization step (Sect. 3.5), i.e. too few suitable background pixels were located in regions of optically thin cloud to effectively characterize the potential fire pixel background. Figure 5 shows box plots of the mean background and potential fire pixel IR3.9 BT and IR3.9–IR10.9 BT difference for this data set. Under clear sky conditions, the median IR3.9 BT for potential active fire pixels is 306.2 K and for the background 303.4 K. Under optically thin cloud, these values decrease to 298.9 and 298.1 K, respectively, and the difference between the IR3.9 BT of fire and non-fire pixels thus

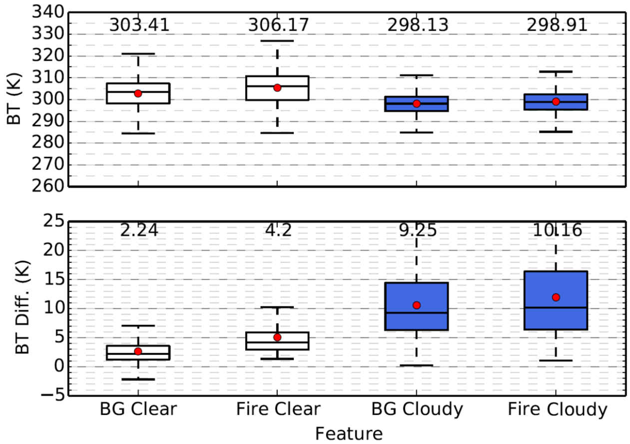


**Figure 5.** Examination of signals from fires burning under clear sky and thin cloud, along with their background (BG) windows. Potential fire pixel (Fire) and BG signal box plots for IR3.9 BT and IR3.9–IR10.8 BT differences calculated using 5 days of SEVIRI daytime data (8–12 August 2014) over Southern Africa. The box plot follows standard conventions, with the bar representing the median and the red dot the mean. The figure above each box plot reports the actual median value.

generally reduces. For the BTD, the median potential active fire pixel signal under clear sky is 4.2 K, and the background 2.2 K. Under optically thin cloud these increase to 10.2 and 9.3 K, respectively, with again generally less difference between the fire and non-fire pixels. These results demonstrate that potential active fire pixels located under optically thin cloud (as defined by the CT mask) often do not produce as strong a contrast with the background as do active fire pixels burning under clear-sky conditions, resulting in the fire signal under optically thin cloud often being too weak for the FTA algorithm to detect. For this reason, no further attempt to detect active fire pixels burning under cloud was made in the current LSA SAF processing chain.

Figure S2 shows an example of the final FRP-PIXEL Quality Product per-pixel classification scheme, where some pixels are classed as containing actively burning fires, but where most pixels are classed as either cloudy or non-cloudy land pixels or "not processed" water pixels (masked even prior to the cloud masking stage). To further minimize the number of false active fire detections caused by unmasked cloud or water, the FTA algorithm originally masked certain pixels immediately neighbouring cloudy pixels or which are within two pixels of a "not processed" water body pixel (masked as "cloud/water edge" (Class 8; Table S1) if they fail to show a strong IR3.9 channel ($\mathrm{BT}_{3.9}$) signal:

$$\mathrm{BT}_{3.9} < 320\,\mathrm{K}. \tag{4}$$

Whilst this test was designed to limit numbers of false fire detections, more recent testing indicated that the adjusted CMa is so effective at detecting clouds that the further cloud-edge test is unnecessary. Its removal successfully reduces errors of omission of active fires with respect to the MODIS active fire products by $\sim 2\,\%$ (FTA algorithm omission errors are around 70 %; see Roberts et al., 2015, for details). Similar testing for the water edge masking showed however that errors of commission increased by $\sim 1\,\%$ on its removal, and so the test was left in place despite it meaning that many fires burning immediately next to water bodies fail to be detected. Water edge pixels are class 11 in the Quality Product (Table S1).

### 3.3 Identification of potential fire pixels (PFPs)

This part of the FTA algorithm (boxed in Fig. 3) identifies all SEVIRI level 1.5 pixels that potentially could contain actively burning fires. First, two spectral thresholding tests related to the IR3.9 ($\mathrm{BT}_{3.9}$) and BTD ($\mathrm{BT}_{3.9} - \mathrm{BT}_{10.8}$) signals must be passed, with thresholds varying with solar zenith angle ($\theta_\mathrm{s}$):

$$\mathrm{BT}_{3.9} > C_{11}\theta_\mathrm{s} + C_{12}, \tag{5}$$

$$\mathrm{BT}_{3.9} - \mathrm{BT}_{10.8} > C_{21}\theta_\mathrm{s} + C_{22}, \tag{6}$$

where $C_{11}$ ($-0.3$ and 0.0), $C_{12}$ (310.5 and 280 K), $C_{21}$ ($-0.0049$ and 0.0), and $C_{22}$ (1.75 and 1.0 K) are constants applied when $\theta_\mathrm{s} > 60°$ and $< 60°$, respectively. The advantage of using these relatively low BT thresholds to discriminate any pixel conceivably containing an active fire is somewhat counteracted by the fact that large areas of homogeneously sun-warmed areas can often also exceed them, leading to significant and unwanted computational demands during subsequent processing stages. To avoid this, a series of standard high pass "edge detecting" spatial filters of $3 \times 3$, $5 \times 5$ and $7 \times 7$ pixel size are applied to the BTD ($\mathrm{BT}_{3.9} - \mathrm{BT}_{10.8}$) image, and each PFP output from Eqs. (5) and (6) must pass the following two tests to remain as a PFP:

$$P = H_\mathrm{filter} \geq DT \times \delta_\mathrm{filter}, \tag{7}$$

$$DT = 2.5 - 0.012 \times \theta_\mathrm{s}, \tag{8}$$

where $H_\mathrm{filter}$ is the output of the high pass spatial filter, and $\delta_\mathrm{filter}$ is a threshold that in the FTA prototype was taken as the standard deviation of the filtered BTD image. To further minimize computational demands during real-time processing, in the operational FTA algorithm $\delta_\mathrm{filter}$ was derived once for each filter size for each daily time slot using four exemplar SEVIRI images, and the minimum $\delta_\mathrm{filter}$ for each time slot and filter size were used in Eq. (7) during operational processing. The dynamic nature of this threshold is now being returned to the operational chain (Fig. 3), since new testing has shown that use of the dynamic threshold reduces active fire detection errors of commission with respect to MODIS by a further 2 % compared to the static case (see Roberts et al., 2015).

### 3.4 Sunglint detection

A sunglint angle ($\theta_g$) is defined for each SEVIRI pixel according to Prins et al. (1998), and those pixels with $\theta_g < 5°$ are coded as glint-affected "Class 4" in the FRP-PIXEL Quality Product (Table S1) and removed prior to the tests described in Sect. 3.3. Two further glint tests are applied after PFP identification to discriminate more ambiguous glint using the ratio of the IR3.9 and VIS0.6 spectral radiances:

$$\frac{L_{3.9}}{L_{0.64}} < \frac{0.7}{p}, \quad (9)$$

$$(2-p)\cdot\frac{L_{3.9}}{L_{10.8}} < 0.0195\,, \quad (10)$$

where $L_{3.9}$, $L_{0.64}$, and $L_{10.8}$ are the spectral radiance of the IR3.9, VIS0.6 and IR10.8 channels, respectively, and $p$ can take a value of either 1 or 2. We assume that the absence of nearby cloud makes it less likely that a particular PFP is caused by glint, so Eqs. (9) and (10) work on the $15 \times 15$ pixel window surrounding each PFP; if this window contains a cloudy pixel, then $p$ is set to 1, otherwise to 2. Pixels satisfying these two tests are coded as "possibly glint affected" (Class 5), whilst all processed pixels not belonging to the PFP set and which have not yet received an alternative classification are coded as Class 0 ("not a potential fire pixel").

### 3.5 Contextual active fire detection

During this stage, an expanding "background window" surrounding each PFP is used to calculate a set of metrics against which the PFP signal is compared, to confirm whether or not it should be classed as a presumed "true" fire pixel. The window starts at $5 \times 5$ pixels and expands until sufficient pixels meet the validity criteria outlined in Roberts and Wooster (2008); namely being cloud free, not a PFP, and passing the following tests which relate, respectively, to not showing the types of spectral signature associated with a possible fire pixel (Eqs. 11, 12), not being affected by the remaining sunglint (Eq. 12), and having spectral signatures less like a fire than that of the PFP under test (Eqs. 14, 15).

$$\frac{L_{3.9}}{L_{10.8}} < 0.0195 \quad (11)$$

$$\mathrm{BT}_{3.9} - \mathrm{BT}_{10.8} < 10\,\mathrm{K} \quad (12)$$

$$\theta_g > 2° \quad (13)$$

$$\mathrm{BT}_{3.9} - \mathrm{BT}_{10.8} < (\mathrm{BT}_{3.9} - \mathrm{BT}_{10.8})_{\mathrm{PFP}} \quad (14)$$

$$\mathrm{BT}_{3.9} < \mathrm{BT}_{\mathrm{PFP}_{3.9}} \quad (15)$$

The terms in the equations above retain their already identified meanings, and $BTD_{\mathrm{PFP}}$ and $\mathrm{BT}_{\mathrm{PFP}_{3.9}}$ are, respectively, the BT difference of the potential fire pixel calculated using the IR3.9 and IR10.8 SEVIRI channels, and the PFP's IR3.9 channel BT.

When defining the operational FTA algorithm, we investigated the detailed characteristics of the aforementioned background window, aiming to elucidate the cause and consequences of certain SEVIRI imaging artefacts that impact the required statistics (e.g. the lowered IR3.9 brightness temperatures seen surrounding certain active fire pixels in Fig. 6). To deliver the anti-aliased properties specified for SEVIRI level 1.5 imagery (Just, 2000; Deneke and Roebeling, 2010), a finite impulse response (FIR) digital filter is applied to each line of SEVIRI data; the filter consists of a symmetric sinc function with 17 coefficients (including some negative coefficients; Fig. 7a) multiplied by a modified Kaiser window function. Such filtering can have particularly significant consequences in areas of high image contrast and to investigate this we convolved the FIR filter with the SEVIRI point spread function (PSF) (Fig. 7b) and applied the result to simulated thermal imagery containing active fires derived at a spatial

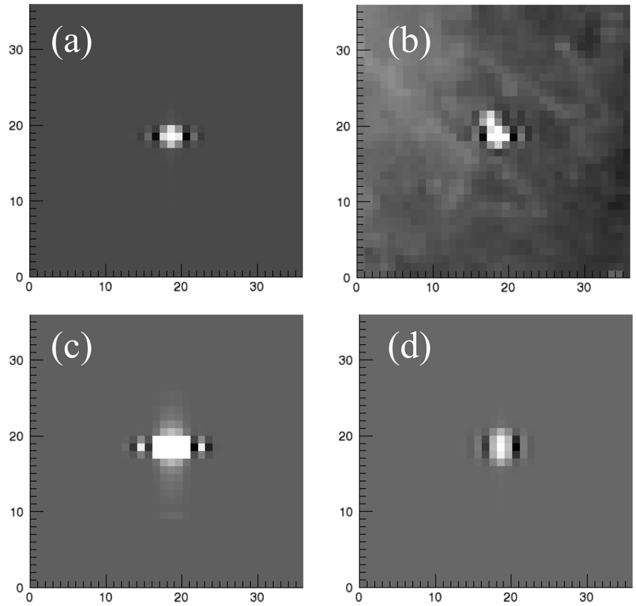


**Figure 6.** Simulated SEVIRI IR3.9 (MWIR) imagery of active fires, shown in comparison to real imagery. Images are scaled with the highest brightness temperature in the images shown as white and the lowest as black. The $x$ and $y$ axes are in SEVIRI image column and row coordinates. **(a)** is a simulated MWIR view of a 350 MW fire contained within the ground area of a single SEVIRI 3 km pixel and with the convolved filter shown in Fig. 7 applied. The fire signal appears smeared across many pixels, and the result appears similar to typical SEVIRI imagery of active fires shown in **(b)** but noting that the dominantly along-scan nature of the smearing may not be so apparent in real SEVIRI imagery due to the pixel geolocation processes performed during the level 1.0 to level 1.5 preprocessing procedures. **(c)** and **(d)** show simulation of larger fires stretching across three 350 MW SEVIRI pixels in the E–W and N–S directions, respectively, with the impact of the filtering shown to be dependent upon the fire orientation with respect to the SEVIRI scan process. The simulations are indicative only, with a uniform surface temperature, atmospheric transmission, and emissivity assumed, and the sub-pixel fire of fixed FRP located at the scene centre.

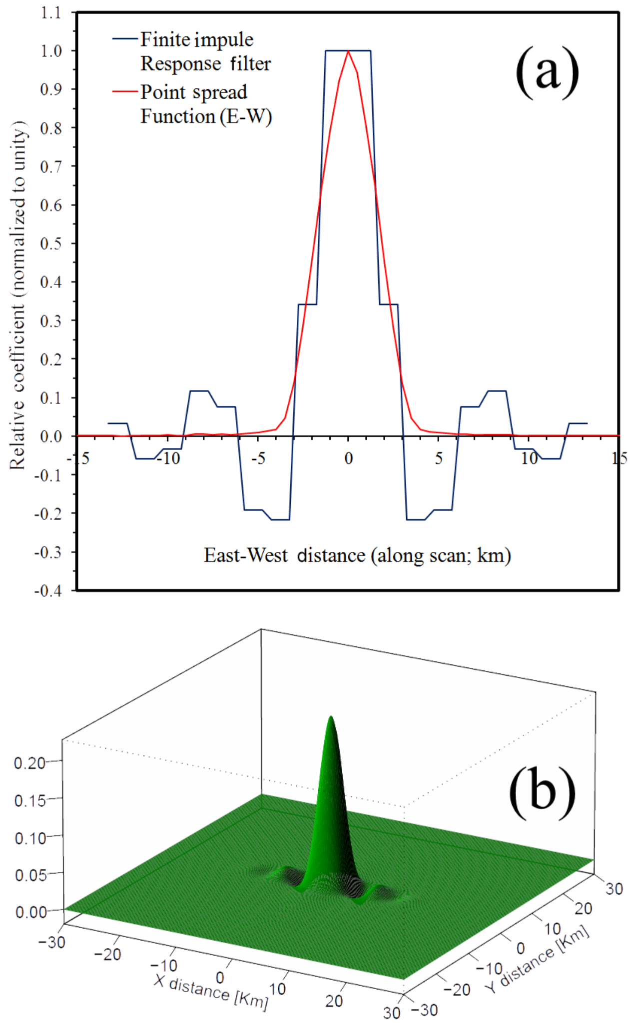


**Figure 7. (a)** The E–W point spread function of SEVIRI (at sub-satellite point) and the finite impulse response (FIR) function. The latter is applied to level 1.0 data before conversion to level 1.5. Both are shown here normalized to unity. Note the negative side lobes of the FIR filter. **(b)** Convolution of the FIR filter and the E–W and N–S SEVIRI point spread function (PSF) used in the simulation of active fire observations (Fig. 6).

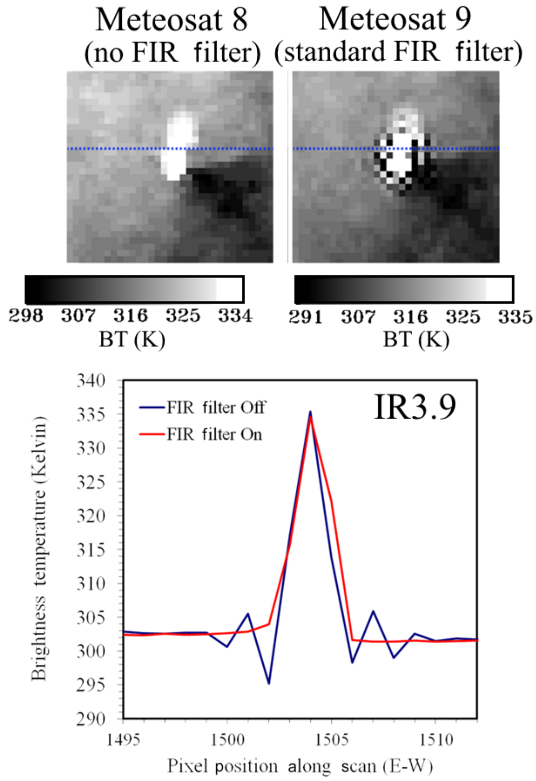


**Figure 8.** Near-simultaneous Meteosat-8 and Meteosat-9 band 4 (MWIR) imagery of a large, intensely burning (high FRP) fire in Southern Africa taken on 3 September 2007 during Meteosat-8 special operations when application of the FIR filter was removed temporarily. The data appear quite different to that collected with the normally operating Meteosat-9.

resolution 10× higher than that of the native SEVIRI pixels. The convolution of the negative coefficients of the FIR filter and the strong IR3.9 channel active fire signals led to substantial decreases in the output IR3.9 channel brightness temperatures, both up- and down-scan of the fire pixel itself (Fig. 6a), an effect mirroring that seen in real level 1.5 SEVIRI data (Fig. 6b).

Further simulations, including of larger fires (e.g. Fig. 7c and d), indicate that the orientation of the fire along or perpendicular to the SEVIRI scan line, including the fire's sub-pixel location, affects the final image details. Freeborn et al. (2014b) recently demonstrated how the sub-pixel fire location affects the MODIS-measured FRP, an effect previously identified with the BIRD (Bispectral Infra-Red Detector) hotspot recognition sensor (Zhukov et al., 2006). Calle et al. (2009) also reported related phenomena in SEVIRI data. Our simulations lead us to conclude that the FIR filter "smearing" of the fire-emitted spectral radiance into neighbouring pixels, and that the depression of the IR3.9 BT of neighbouring pixels can have significant consequences for active fire observations, particularly so if pixels now containing some of the fire-emitted signal are not themselves sufficiently strongly radiating to be detected as active fires (and/or if the background window statistics are unduly contaminated by lowered IR3.9 BTs).

Based on our simulations, we requested a period of Meteosat "special operations", where near-simultaneous data from two MSG satellites could be compared with and without the FIR filter applied. These data are more fully described in Sect. 5.2 and confirm that decreased IR3.9 channel BTs are not seen neighbouring strongly radiating active fire pixels when level 1.5 imagery is pre-processed without the FIR filter being applied (Fig. 8). Further analysis confirms that when calculating the ambient background window statistics for a PFP, excluding the eight pixels immediately

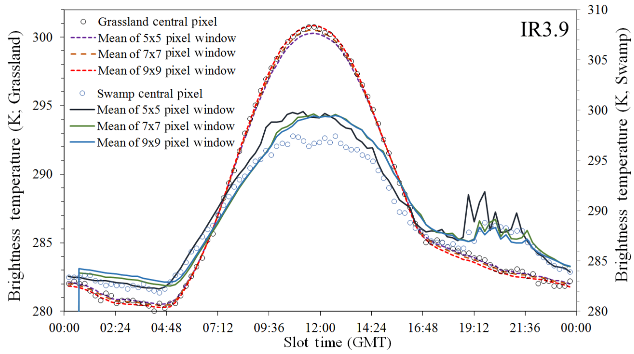


**Figure 9.** Demonstration of the ability to estimate the SEVIRI IR3.9 (MWIR) brightness temperature of the central pixel in a $5 \times 5$, $7 \times 7$ and $9 \times 9$ pixel window using the mean of the remaining "background window" pixels. Results for two different land cover types are shown from the GLC2000 database: grassland (plotted on left-hand $y$ axis) and swamp (plotted on right-hand $y$ axis).

neighbouring the PFP improves the ambient background representation, since these are most affected by the FIR filtering (Fig. 8). This exclusion is implemented in the operational FTA algorithm, as well as the requirement that when $\theta_s > 70°$ any further retained background window pixel must satisfy $BT_{3.9} > 270$ K.

The expanding background window starts at $5 \times 5$ pixels and expands by two in each direction until 65 % of the pixels are considered valid according to the aforementioned criteria (excluding the central $3 \times 3$ pixels). For more than 95 % of PFPs, a $5 \times 5$ window is sufficient to meet this criteria, but expansion up to $15 \times 15$ is allowed. In very rare cases where this is insufficient, the PFP is coded as having "insufficient background pixels" for confirmation as an active fire (Class 6) in the FRP-PIXEL Quality Product (Table S1). In all other cases, a series of statistical metrics derived from the correctly sized background window are used in a set of "spatial contextual" tests to confirm whether the PFP can be classed as a "true fire pixel". These confirmatory tests are fully described in Roberts and Wooster (2008) and remain unaltered in the operational FTA algorithm, so they are not detailed here. They rely on the assumption that the statistical average of the valid background window is representative of the signal the central "PFP" would have had if it had not contained a fire, and this was examined by selecting random nonfire level 1 pixels and re-classifying them as PFPs such that their signals could be compared to those of their background windows (Fig. 9). Apart from GLC2000 pixels classed as swamp, for 80 % of cases examined the mean IR3.9 channel BT of the background window was within 1 K of the central "PFP" pixel $BT_{3.9}$ and always within 2 K. Swamp forms a very small fraction of the SEVIRI disk, and differences here increased up to 6 K, presumably due to spatially varying percentage covers of water and land. Furthermore, in all cases the standard deviation of the background window IR3.9 channel spectral radiance was always larger than the actual difference between that of the central pixel and the window mean, and since the former provides a measure of the background window characterization random error for use during FRP uncertainty specification (Sect. 5.1), this indicates the conservative nature of the resulting uncertainty estimate.

Based on the results of the background window spatial contextual tests, PFPs classed as true fire pixels are coded as Class 1 in the Quality Product (Table S1), and have their FRP derived (Sect. 5). For confirmed fire pixels with a saturated IR3.9 channel signal ($BT_{3.9} \geq 335$ K), FRP is still estimated but with adjustments for channel saturation (Sect. 5.2.1) and the pixel is coded as Class 2. PFPs failing the spatial contextual tests altogether are coded as Class 7 (Table S1). After this, each confirmed fire pixel is given a detection confidence measure (0–1), based on the approach of Giglio et al. (2003) as described in Roberts and Wooster (2008).

## 4 FRP derivation

### 4.1 Derivation of per-pixel FRP values

All confirmed active fire pixels (Classes 1 and 2 in the FRP-PIXEL Quality Product) have their FRP estimated using the MWIR radiance method of Wooster et al. (2003, 2005). This requires quantification of the fires' contribution to the active fire pixels' elevated IR3.9 channel signal and bases this on the difference between the fire pixels' IR3.9 channel spectral radiance ($L_f$) and the mean spectral radiance ($L_b$) of the surrounding background window:

$$\mathrm{FRP} = \frac{\pi \sigma A_n}{\tau_{\mathrm{MWIR}} C_a \cos(\theta_v)} (L_f - L_b), \tag{16}$$

where $L_f$ and $L_b$ have the same units ($\mathrm{mW\,m^{-2}\,sr^{-1}\,(cm^{-1})^{-1}}$), $\tau_{\mathrm{MWIR}}$ is the atmospheric transmittance calculated for the SEVIRI IR3.9 channel, $C_a$ ($\mathrm{mW\,m^{-2}\,sr^{1-}\,(cm^{-1})^{-1}\,K^{-4}}$) is a constant determined according to Wooster et al. (2003, 2005), $\theta_v$ is the view zenith angle (°), and $A_n$ is the SEVIRI ground pixel area at the sub-satellite point (km$^2$).

### 4.2 Method for FRP atmospheric correction

Wooster et al. (2005) demonstrate that the primary atmospheric effect with regard to FRP derivation is the non-unitary MWIR atmospheric transmission ($\tau_{\mathrm{MWIR}}$), that upwelling atmospheric path radiance and reflected downwelling atmospheric radiance can be neglected due to the fire pixel and that the immediately surrounding background area radiances are differenced in Eq. (16). However, the specification of $\tau_{\mathrm{MWIR}}$ is complicated by the fact that the transmittance and fire-emitted spectral radiance signals are far from uniform across the SEVIRI's IR3.9 spectral bandpass.

Figure 10 shows the IR3.9 band spectral response function along with the transmittance of the US standard atmosphere.

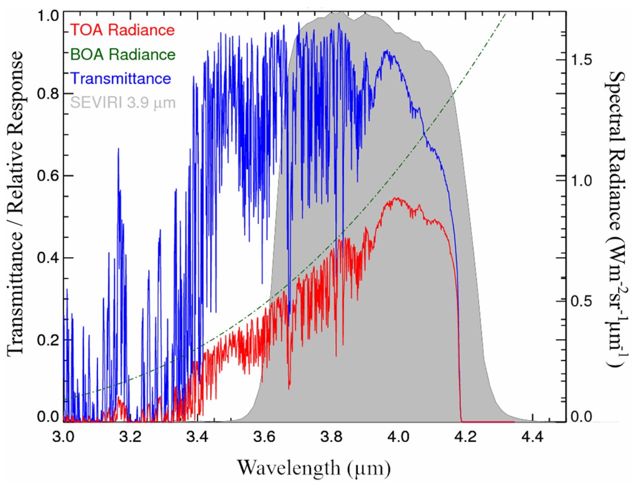


**Figure 10.** SEVIRI IR3.9 (MWIR) band spectral response function, with example atmospheric transmittance calculated across the 3.0–4.5 µm wavelength range assuming a standard atmosphere (Berk et al., 2005), plotted on the left $y$ axis. Also shown, plotted on the right $y$ axis, are the bottom-of-atmosphere (BOA) thermal emittance for a 310 K blackbody, along with the top-of-atmosphere (TOA) equivalent after the emitted radiation has passed through the intervening atmosphere to space. Simulations performed using the MODTRAN5 radiative transfer code (Berk et al., 2005 and the US standard atmosphere).

The impact of the strong $CO_2$ absorption band on overall atmospheric transmission upwards of $\sim 4.0$ µm can be clearly seen, and SEVIRI's IR3.9 band remains sensitive to MWIR radiation at wavelengths longer than 4.2 µm; though, in fact, no surface-emitted radiance reaches the sensor directly at these wavelengths. Many other atmospheric absorption features are seen across the bandpass, many of which depend on the atmospheric total column water vapour (TCWV) content. Also plotted on the right-hand side $y$ axis of Fig. 10 is the bottom-of-atmosphere (BOA) spectral radiance emitted by a 310 K blackbody, along with the equivalent top-of-atmosphere (TOA) measure calculated using MODTRAN5 (MODerate resolution atmospheric TRANsmission; Berk et al., 2005).

When selecting the appropriate atmospheric transmittance to derive a band-integrated TOA radiance signal from a BOA measure, it is quite common to use a band-averaged $\tau_{\mathrm{MWIR}}$ (e.g. Qin and Karnieli, 1999). However, as can be seen in Fig. 10, this not fully appropriate with regard to SEVIRI's IR3.9 band, across which the atmospheric transmittance and ground (and fire)-emitted spectral radiance vary significantly. Specifically, across SEVIRI's IR3.9 band, atmospheric transmittance generally decreases with increasing wavelength, whereas upwelling spectral radiance generally increases. Converting the band-integrated TOA spectral radiance to a BOA measure simply using the mean $\tau_{\mathrm{MWIR}}$ calculated across the IR3.9 spectral bandpass would therefore increase the contribution of the shorter wavelength TOA signal to the band-integrated BOA spectral radiance too much and the longer wavelength signal too little. This effect is more significant here than for narrowband channels such as the MODIS 3.95 µm band 21, because SEVIRI's IR3.9 band has significant sensitivity around the 4.2 µm $CO_2$ absorption region where MWIR atmospheric transmittance at its lowest but the surface-emitted signal is at its highest. Using a band-averaged $\tau_{\mathrm{MWIR}}$ to convert the TOA radiance simulated in Fig. 10 to a BOA signal results in a latter estimate almost 10 % too low, even when the band-averaged transmittance includes consideration of the spectral response function weighting.

In simulations such as those shown in Fig. 10, the spectral shape of the surface-emitted signal and the atmospheric transmittance spectrum are known and can be used to apply the correct transmittance at each observation wavelength. However, true SEVIRI IR3.9 observations do not resolve the incoming signals' spectral behaviour. Therefore, the $\tau_{\mathrm{MWIR}}$ to include in Eq. (16) is best calculated as an effective (or pseudo)- atmospheric transmittance, determined from pre-computed radiative transfer simulations of TOA and BOA fire pixel and background pixel spectral radiance difference signals:

$$\tau_{\mathrm{MWIR}} = \frac{\left[\int_3^5 \widetilde{B(T_\mathrm{f})}^{\mathrm{TOA}} - \int_3^5 \widetilde{B(T_\mathrm{b})}^{\mathrm{TOA}}\right]}{\left[\int_3^5 \widetilde{B(T_\mathrm{f})}^{\mathrm{BOA}} - \int_3^5 \widetilde{B(T_\mathrm{b})}^{\mathrm{BOA}}\right]}, \tag{17}$$

where $\int_3^5 \widetilde{B(T)}$ indicates the spectral radiance calculated using the Planck function at brightness temperature $T$ (K), convolved with the spectral bandpass of the SEVIRI IR3.9 band and integrated over the 3–5 µm spectral range, the subscripts $f$ and $b$ correspond to the fire pixel and the background windows, respectively, and the superscripts BOA and TOA indicate the bottom- and top-of-atmosphere measures.

For the operational LSA SAF processing chain generating the FRP-PIXEL products, Eq. (17) was used to generate a look-up table (LUT) of $\tau_{\mathrm{MWIR}}$ using the RTMOM and latterly the MODTRAN5 atmospheric radiative transfer models (Govaerts, 2006, and Berk et al., 2005, respectively) with varying atmospheric TCWV content ($U_{\mathrm{H_2O}}$; varying between 0.5 and 60 kg m$^{-2}$), view zenith angle ($\theta_\mathrm{v}$), a range of standard atmospheres (tropical, mid-latitude summer, etc.), fire pixel ($T_\mathrm{f}$)- and background pixel ($T_\mathrm{b}$)-integrated brightness temperatures (300–330 and 290–320 K, respectively), aerosol optical thicknesses, and atmospheric $CO_2$ and ozone column amounts. At the latitude/longitude location and view zenith angle ($\theta_\mathrm{v}$) of each confirmed active fire pixel identified by the FRP-PIXEL processing chain, $\tau_{\mathrm{MWIR}}$ is retrieved from this LUT based on the TCWV content taken from ECMWF short-term forecasts available at 0.5° spatial resolution every 3 h. As an example, at the sub-satellite point ($\theta_\mathrm{v} = 0$) for a typical $U_{\mathrm{H_2O}}$ of 20 kg m$^{-2}$ and a mid-latitude summer atmosphere, Eq. (17) indicates $\tau_{\mathrm{MWIR}}$ as 0.69 for use in Eq. (16), compared to 0.74 for the IR3.9 band-averaged value. During this process, the uncertainty in the effective $\tau_{\mathrm{MWIR}}$ ($\sigma_\tau$) is also specified for use in the uncertainly calculations described in Sect. 5.

## 5 FRP uncertainty calculations and the MSG "special operations mode" observation period

### 5.1 FRP uncertainty formulation

A full per-pixel FRP uncertainty ($\sigma_{\mathrm{FRP}}$, MW) is specified at each detected active fire pixel in the FRP-PIXEL product, derived by combining the absolute uncertainties ($\sigma_{V_k}$) of the four variables ($C_\mathrm{a}$, $\tau_{\mathrm{MWIR}}$, $L_\mathrm{f}$, and $L_\mathrm{b}$) of Eq. (16):

$$\sigma_{\mathrm{FRP}} = \mathrm{FRP}\sqrt{\sum_{k=1}^{4}\sigma_{V_k}^2\left(\frac{\partial \mathrm{FRP}}{\partial V_k}\right)^2}, \tag{18}$$

where $V_k$ represents the variables of Eq. (16) ($C_\mathrm{a}$, $\tau_{\mathrm{MWIR}}$, $L_\mathrm{f}$ and $L_\mathrm{b}$, respectively,) and where the absolute uncertainties ($\sigma_{V_k}$) in these are assumed uncorrelated. Solving for the partial derivatives in Eq. (18) gives

$$\sigma_{\mathrm{FRP}} = \mathrm{FRP}\left[\left(\frac{\sigma_{C_\mathrm{a}}}{C_\mathrm{a}}\right)^2 + \left(\frac{\sigma_{\tau_{\mathrm{MWIR}}}}{\tau_{\mathrm{MWIR}}}\right)^2 + \left(\frac{\sigma_{L_\mathrm{b}}}{L_\mathrm{f}-L_\mathrm{b}}\right)^2 + \left(\frac{\sigma_{L_\mathrm{f}}}{L_f-L_\mathrm{b}}\right)^2\right]^{1/2}, \tag{19}$$

where each term takes the following values.

$\sigma_{C_\mathrm{a}}$ is the variability in the $C_\mathrm{a}$ "FRP coefficient" ($\mathrm{mW\,m^{-2}\,sr^{-1}\,(cm^{-1})^{-1}\,K^{-4}}$) used in Eq. (16), which across the specified active fire temperature range of 650–1350 K equates to a $\left(\sigma_{C_\mathrm{a}}/C_\mathrm{a}\right)$ value of $\sim 10\,\%$ (Wooster et al., 2005).

$\sigma_{\tau_{\mathrm{MWIR}}}$ is the variability in calculated atmospheric transmissivity, specified in Sect. 4.2 and resulting from uncertainties in the TCWV and in other atmospheric parameters used in the radiative transfer modelling.

$\sigma_{L_\mathrm{b}}$ is the standard deviation of the background window pixels' spectral radiance ($\mathrm{mW\,m^{-2}\,sr^{-1}\,(cm^{-1})^{-1}}$), calculated as discussed in Sect. 3.5 and adjusted for the atmospheric pseudo-transmittance ($\tau_{\mathrm{MWIR}}$).

$\sigma_{L_\mathrm{f}}$ is the uncertainty in the measured fire pixel spectral radiance ($\mathrm{mW\,m^{-2}\,sr^{-1}\,(cm^{-1})^{-1}}$) resulting from a combination of (i) the SEVIRI sensors' radiometric noise ($\sigma_L$), (ii) instances of IR3.9 band sensor saturation ($\sigma_S$), and (iii) influences from the pre-processing steps used to generate the SEVIRI level 1.5 data from the raw observations (termed here $\varepsilon_p$), for example, the application of the FIR filter detailed in Sect. 3.5. These three contributions are represented by the three fractional terms of Eq. (20), where $L_\mathrm{f}$ remains the measured radiance of the active fire pixel ($\mathrm{mW\,m^{-2}\,sr^{-1}\,(cm^{-1})^{-1}}$) and $S$ is its estimated adjusted radiance in the case of IR3.9 channel saturation (see Sect. 5.2.1 for specification of $S$ and $\sigma_S$):

$$\sigma_{L_\mathrm{f}} = L_\mathrm{f}\sqrt{\left[\left(\frac{\sigma_L}{L_\mathrm{f}}\right)^2 + \left(\frac{\sigma_S}{S}\right)^2 + \varepsilon_p^2\right]}. \tag{20}$$

The "end of life" radiometric noise prediction of the SEVIRI IR3.9 channel is 0.17 K (Schmetz et al., 2002; Hewison and Muller, 2013), translating to $\sigma_L = 0.038\,\mathrm{mW\,m^{-2}\,sr^{-1}\,cm^{-1}}$ $(0.025\,\mathrm{W\,m^{-2}\,sr^{-1}\,\mu m^{-1}})$. To specify the remaining terms, a series of unique Meteosat-8 SEVIRI observations were made.

### 5.2 Meteosat-8 special operations mode: data collection and analysis

Between 3 and 7 September 2007, Meteosat-8 was operated in "rapid scan" mode, imaging every 4 min between 3° N and 33° S, with a cycle of additional adjustments:

- "low gain" operation of the IR3.9 channel, allowing for measurements to 375 K;
- alteration of the Meteosat main detection unit (MDU) standard SEVIRI FIR filter (Fig. 7) to a 1-pixel-wide rectangular "top-hat" function that allows the original observations to be transmitted to the primary ground station for use in level 1.5 data generation.

The Meteosat-8 special operations period was aimed at both assessing the individual uncertainty terms in Eq. (20), and their aggregate effect. Near-simultaneous observations from the normally operating Meteosat-9 were acquired for comparison.

#### 5.2.1 Effect of IR3.9 band saturation

SEVIRI saturates at a digital number (DN) of 1023, equating to an IR3.9 channel brightness temperature ($\mathrm{BT}_{3.9}$) of just over 335 K ($\sim 3.6\,\mathrm{mW\,m^{-2}\,sr^{-1}\,(cm^{-1})^{-1}}$) in standard operating mode. Roberts and Wooster (2008) reported that IR3.9 saturation normally occurs in no more than a few percent of level 1.5 active fire pixels, coded as Class 2 in the FRP-PIXEL Quality Product (Table S1). Although such pixels share the same $\mathrm{BT}_{3.9}$, application of Eq. (16) would not necessarily give them the same FRP, since this depends also on the background window radiance, pixel area (and thus $\theta_\mathrm{v}$) and $\tau_{\mathrm{MWIR}}$. Around the SSP, IR3.9 saturation occasionally occurs at FRPs as low as 45 MW, if the fire is burning in a particularly warm daytime background ($\geq 330$ K), but more typically at $\sim 250$ MW. Further from the SSP, FRPs of more than double this can be measured without saturation. Our primary aim was to determine which FRP ($S$) to record at saturated IR3.9 pixels, and with what uncertainty ($\sigma_S$), used in Eq. (20). Barnie et al. (2015) tackled a similar problem with respect to volcanic thermal features.

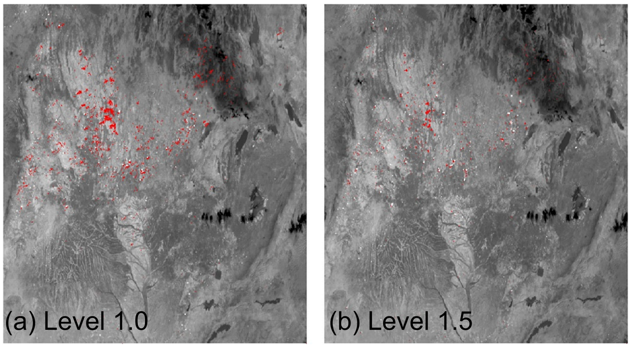


**Figure 11.** Impact of IR3.9 channel saturation in SEVIRI level 1.0 and level 1.5 data. Typically, a maximum of only a few percent of active fire pixels are saturated in any particular SEVIRI image, but the exact proportion is dependent on data pre-processing levels. Here, in red we show the spatial distribution of saturated active fire pixels in **(a)** level 1.0 and **(b)** level 1.5 SEVIRI data collected over a 2-day (48 h) period in a region of Southern Africa (16 and 17 July 2014). Twice as many pixels are saturated in the level 1.0 over these 2 days (shown by a 10-bit DN of 1023; $n = 2797$) than are apparent in the level 1.5 data (shown by a maximum brightness temperature recordable in the IR3.9 band; $n = 1390$). The background imagery on which the saturated pixels are displayed is an IR3.9 image acquired on 17 July at 13:00 UTC.

We first explored the impact of the level 1.0 to level 1.5 IMPF conversion procedures, which involve geometrically resampling data using a bi-cubic function. We found IR3.9 saturation to be more prevalent in the level 1.0 data, as the resampling has the effect of smearing some fire pixel signals from saturated to unsaturated (Fig. 11). We used the Meteosat-8 special operations data that included a period of low-gain IR3.9 operations to quantify the impact further. When the IMPF used a nearest neighbour geometric resampling scheme, rather than the standard resampling scheme, the resulting level 1.5 data showed not a single saturation event, with the highest IR3.9 signal being 6.7 mW m$^{-2}$ sr$^{-1}$ (cm$^{-1}$)$^{1}$ (373 K) and an FRP of 1989 MW (Eq. 16 at $\theta_\mathrm{v}$ of 14°). Figure 12a shows the frequency distribution of per-pixel FRP recorded at active fire pixels detected in level 1.5 data that would normally have been saturated under standard SEVIRI operations. Artificially capping the IR3.9 brightness temperatures of these pixels at the standard 335 K saturation temperature and recalculating their FRP using Eq. (16) allowed for a FRP comparison of these "simulated saturated" data to that from the unsaturated (low-gain) observations. Not unexpectedly, the greatest impact of IR3.9 band saturation occurs near the peak of the typical fire diurnal cycle seen in Fig. 2, when around 5 % of the level 1.5 pixels would have been saturated under "standard" operations and where total Southern Africa FRP would consequently be underestimated by around 13 %. At night these values change to a maximum of 4 and 5 %, respectively; moreover, since regional FRP at night is typically very low (Fig. 2), the absolute amount of FRP underestimation at night is rather negligible. The data shown in Fig. 12, along with the equivalent derived from our simulated saturated data, were used to provide the replacement IR3.9 band spectral radiance for saturated pixels (specified as $S$ and the associated uncertainty $\sigma_S$ in Eq. 20) that are coded as 2 in the Quality Product (Table S1), which was also used to replace $L_\mathrm{f}$ in Eq. (16). $S$ and $\sigma_S$ were based on the median (4.08 mW m$^{-2}$ sr$^{-1}$ (cm$^{-1}$)$^{-1}$) and median absolute deviation from the median (0.49 mW m$^{-2}$ sr$^{-1}$ (cm$^{-1}$)$^{-1}$) of the IR3.9 spectral radiances of Fig. 12, rather than the mean and standard deviation, due to the non-normal distribution. Figure 12b shows the resulting data, stratified by $\theta_\mathrm{v}$ (intervals 25–30° and 30–35° contain the vast bulk (79 %) of the data). Since pixel area and atmospheric transmittance increase with $\theta_\mathrm{v}$, the FRP of pixels that would saturate under standard operating conditions generally increases with $\theta_\mathrm{v}$. For each fire pixel that would normally be saturated, replacing their actual spectral radiance with $S$ and specifying the uncertainty $\sigma_S$ gives a "predicted" median FRP for each $\theta_\mathrm{v}$ interval that is a reasonable fit to the observed distribution calculated using the unsaturated IR3.9 observations made during the special operations period. Thus, under normal operations, the use of this saturation adjustment provides an estimate of FRP closer to the real emitted FRP than would be the case if the pixels' saturated radiance measures had been maintained.

### 5.2.2 Impact of SEVIRI level 1.0 to 1.5 conversion

Raw SEVIRI data undergoes pre-processing prior to its conversion to level 1.5 data (Sect. 2.2). To assess the impacts of the SEVIRI pre-processing (Sect. 2.2) we again used Meteosat-8 special operations data, specifically for when the onboard and on-ground processing chain of SEVIRI was altered to replace the standard FIR filter with the top-hat rectangular filter of single pixel width, and where the level 1.5 data were delivered using both bi-cubic and nearest neighbour geometric resampling schemes. Meteosat-8 and Meteosat-9 level 1.5 standard mode full disk data intercomparisons were undertaken first to elucidate initial differences between the two sensors. Using simultaneous observations of over 35 000 active fire pixels, Meteosat-8 was found to measure IR3.9 spectral radiances on average $1.0 \pm 7.7$ % (mean $\pm$ standard deviation) lower than Meteosat-9 (Fig. 13), with the bias most likely the result of Meteosat-9 being positioned 3.4° further west than Meteosat-8 and thus with a different view zenith angle and ground pixel area. The variability likely stems from different sub-pixel positions of the fires, whose impact was illustrated in Freeborn et al. (2014c) for MODIS. The degree of difference changed as the special operations rapid-scan Meteosat-8 data were substituted with observations now being made approximately 1 min apart due to the different scanning schemes used on the two satellites. From these data, the separate uncertainty coming from the measurement time differences and the differing

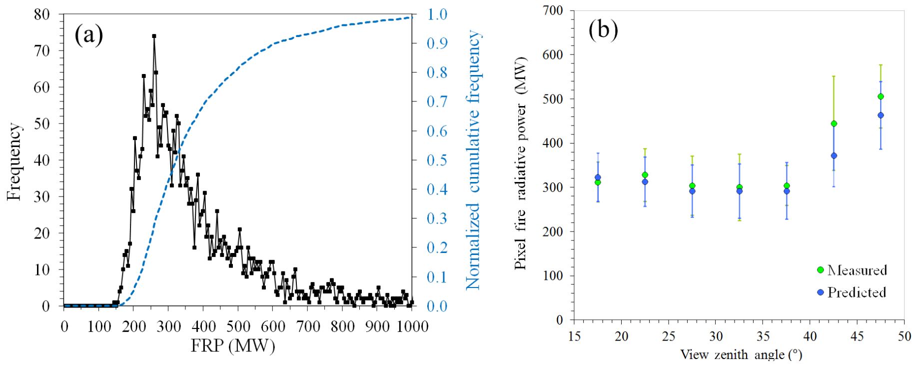


**Figure 12.** Occurrence and impact of SEVIRI IR3.9 saturation. **(a)** Frequency distribution and normalized cumulative frequency of the FRP recorded at detected active fire pixels that would have been saturated under normal SEVIRI operating conditions but which remained unsaturated during the low-gain special operation of the IR3.9 band of Meteosat-8 SEVIRI. Pixels with FRP > 1000 MW are shown due to their extremely low frequency, though one pixel with an FRP approaching 2000 MW was seen (see main text). **(b)** Median FRP recorded at active fire pixels which would have been saturated had Meteosat-8 SEVIRI been operating in normal gain mode but which when observed during the low-gain IR3.9 band special operation of Meteosat-8 SEVIRI remained unsaturated. Data are stratified by view zenith angle. Also shown are the $\pm 1$ mean absolute deviation from the median and the predictions of FRP made when the actual fire pixel IR3.9 spectral radiance is replaced with a fixed value of 4.08 mW m$^{-2}$ sr$^{-1}$ (cm$^{-1}$)$^{-1}$ to represent the adjustment applied to saturated pixels in normal mode level 1.5 SEVIRI data during FRP-PIXEL processing (see Sect. 5).

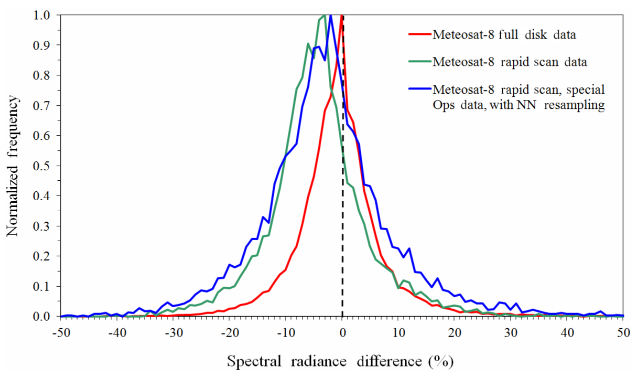


**Figure 13.** Comparison of SEVIRI IR3.9 band spectral radiance differences recorded at active fire pixels observed simultaneously by Meteosat-9 operated in standard mode full disk viewing and Meteosat-8 operated in both standard mode and a number of special operation modes. The red line shows the difference between Meteosat-8 and Meteosat-9 signals when the former is operated in normal mode, with no time difference between observations; the green line shows when Meteosat-8 rapid scan mode was used, which resulted in time differences of 50–65 s between matched observations of the two satellites; the blue line shows when Meteosat-8 rapid scan data were processed without the FIR filter and with a nearest neighbour geometric resampling scheme (rather than the normal bi-cubic function). From these intercomparisons, estimates of the radiometric uncertainties introduced by the SEVIRI level 1.0 to level 1.5 pre-processing operations were deduced for use in FRP uncertainty specification (Sect. 5).

data processing chains were calculated, and the uncertainty impact of the level 1.0 to level 1.5 processing operations ($\varepsilon_p$) was estimated as 0.084 (8.4 %) for use in Eq. (20).

To illustrate of the impact that different SEVIRI pre-processing operations can have on the active fire data, Fig. 14 includes “total scene” FRP comparisons of Meteosat-8 data processed using the standard FIR (sinc) and top-hat filters and nearest neighbour and bi-cubic geometric resampling schemes. The top-hat filter allows lower FRP active fire pixels to be detected, giving a lower minimum total scene FRP than is obtained when applying the standard FIR filter (which tends to “smear” fire pixel radiances). The geometric resampling scheme used also impacts total scene FRP to a greater extent when the FIR filter is applied, with larger impacts for scenes containing only relatively few lower FRP active fire pixels (upon whose detectability the filter selection will impact most strongly). Further investigation shows that the radiometric uncertainty of the active fire pixel radiance is the largest contributor to the overall FRP uncertainty defined by Eq. (19) and that consideration should be given to optimizing SEVIRI level 1.0 to level 1.5 pre-processing operations with respect to active fire data in order to minimize this.

## 6 LSA SAF SEVIRI FRP-GRID product

### Product justification, derivation, and implementation

Whilst Sect. 5 shows that some optimization of the IMPF level 1.5 data pre-processing chain could still be made for the active fire application, when viewing the same ground area at the same time (as occurs a few times per day), MODIS (with a higher spatial resolution and higher MWIR band saturation limit) will generally offer a better opportunity to detect the true regional-scale FRP of landscape-scale fires than SEVIRI. A comparison of the frequency–magnitude distribution

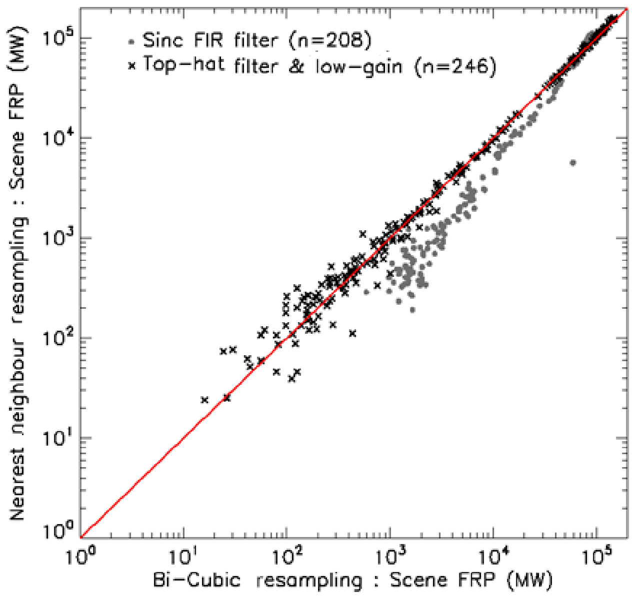


**Figure 14.** Cumulative FRP (MW) in a scene as measured by Meteosat-8 operating in special operations mode across the region of the rapid scan observations (3° N–33° S) when data were delivered using different geometric resampling schemes (nearest neighbour and bi-cubic convolution) and image processing filters (standard sinc function shown in Fig. 7 and top hat, which equates to no significant digital filtering). Data were collected between 3 and 7 September 2007.

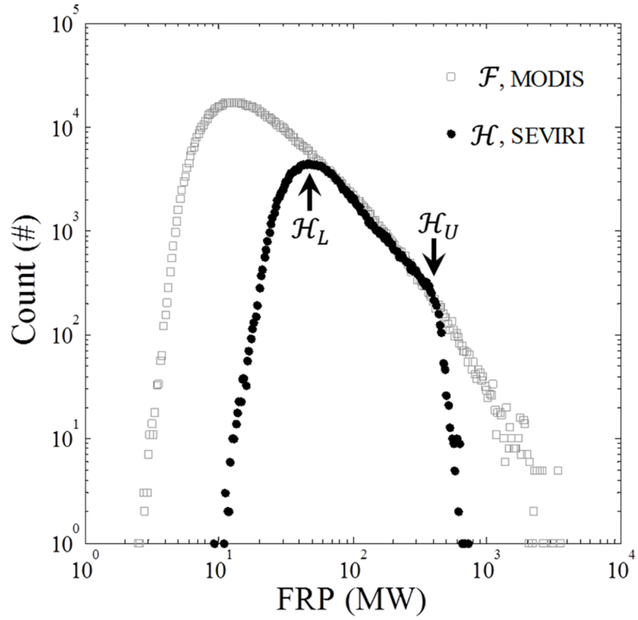


**Figure 15.** Frequency–magnitude distributions constructed from coincident active fire pixels detected by SEVIRI, $H$ (•) and MODIS, $F$ (□) over the African continent between May 2008 and May 2009. The lower breakpoint of the SEVIRI distribution, $H_L$, coincides with the decline in SEVIRI's active fire detection performance as the thermal radiance emitted from small and/or lower intensity fires cannot be reliably distinguished from that of the background window, so many remain undetected. The upper breakpoint, $H_L$, coincides with the onset of IR3.9 detector saturation. The Level 3 FRP-GRID product aims to account for the FRP that SEVIRI fails to detect as a result of these sensor artefacts as well as by that due to cloud obscuration.

of concurrent and collocated SEVIRI and MODIS FRP observations indicates the notable biases of SEVIRI (Fig. 15). SEVIRI's statistical distribution of measured per-pixel FRP ($H$) is skewed to the right and can be divided into three broad regimes. Between $H_L$ and $H_U$, the distribution follows a power law, with SEVIRI detecting fewer active fire pixels with increasing FRP owing to the true rarity of extreme (high FRP) fire behaviour on the landscape. In the lower regime (below $\sim$30–40 MW), $H$ deviates from this power-law as the performance of the FTA algorithm applied to SEVIRI is increasingly limited by the fact that low FRP fires are increasingly difficult to distinguish above the ambient background variability and many thus remain undetected. Roberts et al. (2015) provide a full assessment of this effect using scene-to-scene comparisons between SEVIRI FRP-PIXEL products and MODIS active fire data. Finally, above $H_U$ SEVIRI's per-pixel FRP distribution suffers from right-hand truncation due to IR3.9 band saturation, albeit in the final FRP-PIXEL product this is adjusted for using the methods detailed in Sect. 5.2.1.

The above issues lead to a general underestimation of regional-scale FRP totals measured by SEVIRI when compared to simultaneously recoded MODIS data (Roberts and Wooster, 2008; Roberts et al., 2015). Providing adjustment for this and for varying levels of cloud cover, whilst maintaining a temporal resolution still significantly higher than that offered by polar orbiting systems, is the role of the SEVIRI Level 3 FRP-GRID product. The product combines information contained within all FRP-PIXEL files collected each hour, and delivers a cloud-cover and bias-adjusted, spatiotemporal full-disk summary product at a 5° h$^{-1}$ resolution (Fig. 16).

Freeborn et al. (2009) indicated that, in general, when viewing African areas simultaneously, MODIS measures on average approximately twice the FRP measured by SEVIRI. However, large regional and temporal differences exist, and Freeborn et al. (2014a) recently demonstrated that over smaller 1° areas within a single country (in this case the Central African Republic, one of the most fire-affected African countries) SEVIRI's active fire error of omission with respect to MODIS varies between 25 and 74 % (depending on the locations fire regime), causing a similar variation in the degree of FRP underestimation. It is clear from such analysis that spatially varying bias-adjustment factors are required in the FRP-GRID product, and these were derived using a set of coincident SEVIRI and MODIS active fire observations (May 2008–May 2009), with both data sets

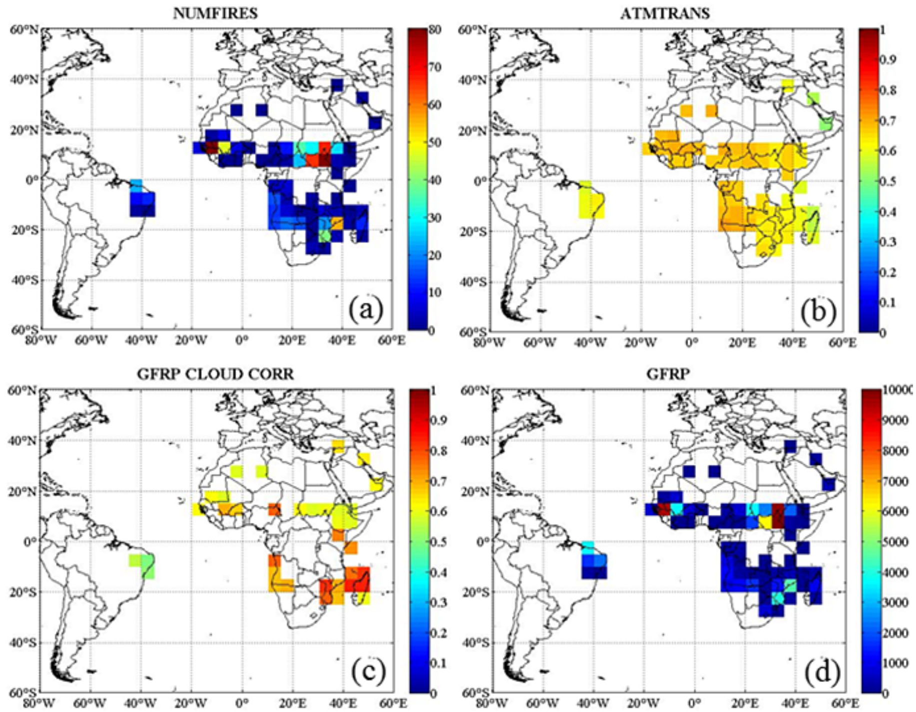


**Figure 16.** Example of the product contents for a single FRP-GRID product (issued hourly), as recorded on 11 November 2009 at 14:00 UTC, including **(a)** the average number of fires detected per 15 min imaging time slot, **(b)** the average atmospheric correction factor, **(c)** the average cloud correction factor, and **(d)** an estimate of the average FRP that MODIS would have measured during the hour. A full description of all FRP-GRID product fields is provided in Table S2.

atmospherically corrected using the Sect. 4.2 scheme. SEVIRI active fire pixels were accumulated over 1 h, and, to achieve a sufficient active fire pixel sample size, matching MODIS and SEVIRI active fire detections were accumulated within 5° grid cells. To minimize MODIS edge-of-scan effects (Freeborn et al., 2009, 2011, 2014b) only MODIS data within the centre two thirds of the swath were used. Half the resulting data were used as the training data set and half for the performance evaluation reported in Roberts et al. (2015). Figure 17 illustrates the methodology, with the summed atmospherically corrected FRP measured by MODIS within each 5° grid cell ($\sum \mathrm{FRP}_G$) related to that measured by SEVIRI using

$$\sum \mathrm{FRP}_G = \alpha_{\mathrm{ROI}} \left( \frac{1}{n} \sum_{t=1}^{n} \sum \mathrm{FRP}_{\mathrm{SEVIRI},t} \right)^{\beta_{\mathrm{ROI}}}, \tag{21}$$

where the value in parenthesis on the right-hand side represents the atmospherically corrected sum of FRP measured by SEVIRI in the 5° cells averaged over the $n$ preceding time slots available in 1 h (where $n = 4$, typically) and the factors $\alpha$ and $\beta$ are power law parameters. The spatial variation was considered by calculating these factors separately for each of the four LSA SAF geographic regions. Equation (22) therefore converts aggregate SEVIRI-derived FRP measures into those which would have been measured by MODIS when viewing the area within the centre two-thirds of its swath. The exponent $\beta$ was functionally intended to allow for the fact that SEVIRI / MODIS ratios of FRP are generally lower during periods of reduced fire activity (Freeborn et al., 2014a); however, the predictive abilities of this formulation proved to be no more skilful than a linear formulation, so $\beta$ was fixed at 1.0 and $\alpha$ derived using a weighted least squares linear best fit to the median values of the training data set (Fig. 17). Final values of $\alpha$ (and standard error) used in the FRP-GRID product are 1.674 (0.062), 1.464 (0.065), 2.057 (0.224), and 1.674 (0.173) for NAfr, SAfr, SAme, and Euro, respectively. Moreover, since the value for the European LSA SAF region was found statistically insignificantly different from that of Northern Africa, it was assigned the same value given that many more fires were available in Northern Africa to enhance relationship robustness.

Uncertainty ($\sigma_G$) on the derived gridded FRP is specified as

$$\sigma_G = \sqrt{\sum_{k=1}^{2} \left( \frac{\partial G}{\partial V_k} \right)^2 \sigma_{V_k}^2}, \tag{22}$$

where $V_k$ represents the variables of Eq. (22) contributing to the uncertainty in $G$, namely the coefficient $\alpha$ and the mean FRP measured by SEVIRI in the grid cell over a 1 h

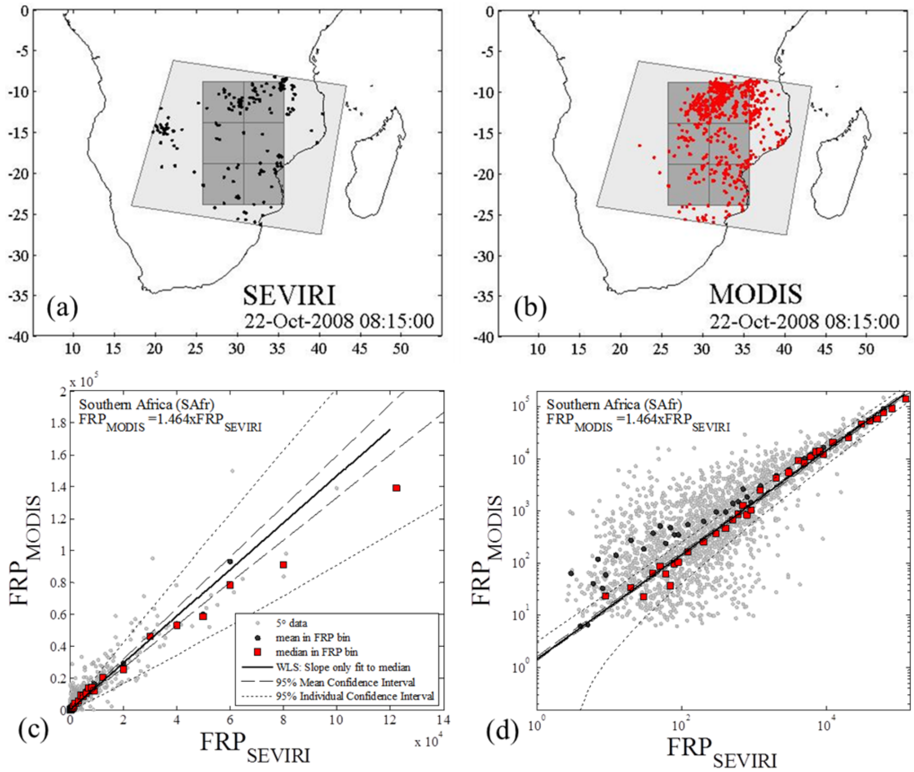


**Figure 17.** Illustration of the training data set and technique used to derive the regional bias adjustment factors used in generating the FRP-GRID product, here illustrated for the Southern African LSA SAF region. Temporally coincident **(a)** SEVIRI and **(b)** MODIS active fire pixels between May 2008 and May 2009 were accumulated in 5° grid cells strategically located within geographic areas covered by the centre two-thirds of the MODIS swath. Shown is one example obtained at 08:15 UTC on 22 October 2008. To achieve a sufficient sample size, SEVIRI active fire pixels in 5° cells were averaged over an hour, as in the FRP-GRID product. These hourly values (grey circles) were binned and the result compared to the median (red squares) and mean (black circles) of the MODIS observations. Appropriate SEVIRI-to-MODIS bias adjustment coefficients were determined by performing a weighted linear least squares fit through the median values, shown in **(c)** on a linear scale and in **(d)** on a log scale (here for the SAfr region only). The resulting factors are applied in the FRP-GRID processing chain.

summation period. Expanding this expression,

$$\sigma_G = G\sqrt{\left(\frac{\sigma_{\alpha_{\mathrm{ROI}}}}{\alpha_{\mathrm{ROI}}}\right)^2 + \left(\frac{\sqrt{\sum_{i=1}^{p}\sigma^2_{\mathrm{FRP},i}}}{\sum_{t=1}^{n}\mathrm{FRP}_{\mathrm{SEVIRI},t}}\right)^2}, \tag{23}$$

where $\sigma_{\alpha_{\mathrm{ROI}}}$ is the uncertainty in $\alpha$, $p$ is the number of active fire pixels detected by SEVIRI in the grid cell during the hour, and $\sigma_{\mathrm{FRP},i}$ is the uncertainty associated with the individual active fire pixel $i$ given by Eq. (19) and stored in the FRP-PIXEL product.

The FRP-GRID algorithm also bias adjusts the hourly averaged FRP by normalizing by the hourly averaged cloud cover fraction. This procedure is similar to that performed for MODIS by Giglio et al. (2006) and in Global Fire Assimilation System (GFAS) of the Copernicus Atmosphere Monitoring Service (Kaiser et al., 2012). It is important to stress that the bias and cloud-cover adjustment procedures implemented during FRP-GRID processing are purely statistical in nature and aimed at reducing the impact of regional-scale biases occurring when data are accumulated over multiple time slots. Importantly, the cumulative FRP detected by the original FRP-PIXEL products is obtainable from the FRP-GRID product, so that the user can remove, adjust, or apply their own bias corrections should they prefer. The data sets stored in the FRP-GRID files are shown in Table S2, but many users may wish simply to focus on using the FRP-PIXEL product itself.

## 7 Product comparison and trend analysis

### 7.1 Comparison to other SEVIRI active fire products

Since Roberts et al. (2005) published the first Meteosat SEVIRI active fire detection algorithm, other active fire studies have made use of SEVIRI data (e.g. Calle et al., 2006; Amraoui et al., 2010; Roberts and Wooster, 2014), some of which have resulted in routinely generated data sets (e.g.

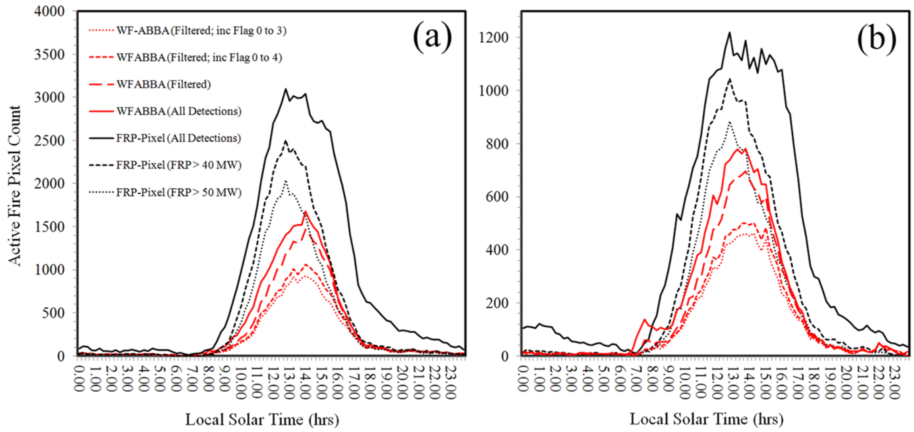


**Figure 18.** Comparison between FRP-PIXEL product active fire detections made across Southern Africa (the LSA SAF SAfr region; Fig. S1), along with those made simultaneously by the WF-ABBA SEVIRI fire product (Gonzalo et al., 2009; http://wfabba.ssec.wisc.edu/). Dates are **(a)** 2 August 2014 and **(b)** 31 August 2014, and both are shown in terms of local solar time of detection. For the FRP-PIXEL product, three active fire time series are shown: all detections, and those only from fire pixels with FRP > 40 MW and > 50 MW, since it is known that significant undercounting of active fire pixels occurs around these limits (i.e. below threshold $H_L$ in Fig. 15). For the WF-ABBA active fire detections, four versions of the data are shown: all active fire detections, the WF-ABBA "filtered" detections where SEVIRI pixels only detected an active fire once during 24 h are removed, and the filtered detections keeping only the higher possibility fires (WF-ABBA flags 0–3), and high and medium possibility fires (WF-ABBA flags 0–4). Details of the WF-ABBA flags can be found at www.ssd.noaa.gov/PS/FIRE/Layers/ABBA/abba.html. On both days and at all time slots, the full FRP-PIXEL product active fire record (black line) detects substantially greater numbers of active fire pixels than the full WF-ABBA record (red line). Roberts et al. (2015) go on to further compare the performance of these two products to MODIS active fire records.

Carvalheiro et al., 2010; Calle et al., 2011). Roberts et al. (2015) report a detailed performance comparison and evaluation of many of these products compared to FRP-PIXEL, and Fig. 18 demonstrates the magnitude of the differences that can occur, here between the WF-ABBA (Wildfire Automated Biomass Burning Algorithm) and FRP-PIXEL products derived from the same level 1.5 data. Since we know that the FRP-PIXEL product undercounts active fire pixels below the $H_L$ threshold of Fig. 15, we show both the total FRP-PIXEL fire pixel count at each time slot, and that from pixels with FRP > 40 MW and > 50 MW. For many imaging slots, the FRP-PIXEL product detects around twice as many active fire pixels as does WF-ABBA, even when using the "all detections" (unfiltered) WF-ABBA data. The latter appear also to show some potentially unrealistic temporal patterns, for example in Fig. 18b during the early morning of 31 August 2014 a local peak in fire pixel count is present at 07:00 local time and is quite possibly caused by glint effects. This local peak is reduced and finally removed by the more stringent WF-ABBA filtering, though this filtering also lowers the number of overall fire pixels recorded. Roberts et al. (2015) includes a much more complete active fire product intercomparison and performance evaluation, but the limited comparison provided here serves to indicate both the highly sensitive nature of the FTA algorithm and its ability to screen out early morning sunglint induced false alarms without recourse to temporal filtering. Since fires in African landscapes quite often show up in a given pixel only once in a 24 h period (either having moved into a neighbouring pixel as the fire spreads across the landscape, or being detected only occasionally due to the low FRP nature of the fire itself), the ability to perform sensitive and accurate active fire detection without having to filter out fire pixels detected only once during the day offers a useful capability.

### 7.2 Comparison to MODIS and analysis of active fire trends

The LSA SAF Meteosat SEVIRI FRP products have been available since 2008 and in 2015/2016 a reprocessing is planned that will generate over a decade of data. Baldassarre et al. (2015) and Roberts et al. (2015) show how these products can be used to support fuel consumption rate estimation for use in high temporal resolution atmospheric modelling of smoke plume dispersion, whilst Freeborn et al. (2014a, c) demonstrate both their complementarity to MODIS and their ability to discriminate trends in fire behaviour. Figure 19 builds on this to show (a) MODIS MOD14/MYD14 and (b, c) SEVIRI FRP-PIXEL active fire detections collected over the Central African Republic. The nearest temporally coincident SEVIRI active fire pixel for each MODIS active fire pixel was calculated based on the ground distance $\Delta d$ between the pixel centres. Results indicate that 30, 42, and 53 % of the MODIS active fire pixels had a SEVIRI counterpart detected at the same time (i.e. those in Fig. 19b) and located within 3, 4, and 5 km, respectively, and only 10 % had the spatially closest, simultaneously detected SEVIRI

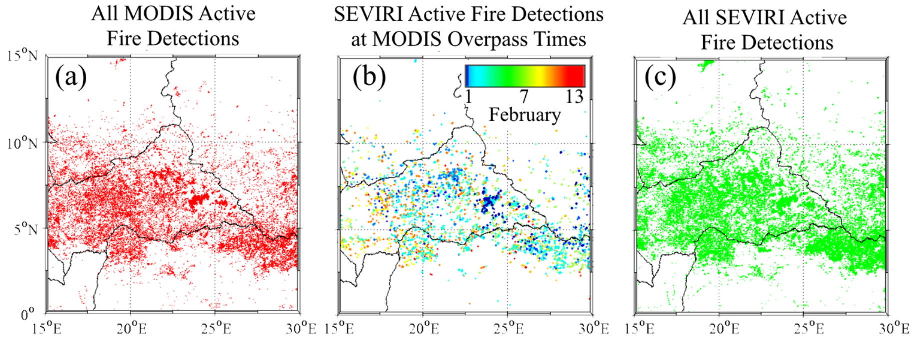


**Figure 19.** Active fire detections made across a 15° × 15° region covering the Central African Republic during a 2-week window (1–13 February 2004), as detected from **(a)** the MOD14/MYD14 active fire products, **(b)** SEVIRI data and the FTA algorithm within ±6 min of the MODIS overpass, and **(c)** all SEVIRI data. In **(b)**, the detected active fire pixels are coloured by day of detection and it is apparent that fires appear potentially larger and are detected earlier in the east, somewhat matching the detailed analysis presented in Freeborn et al. (2004a, c).

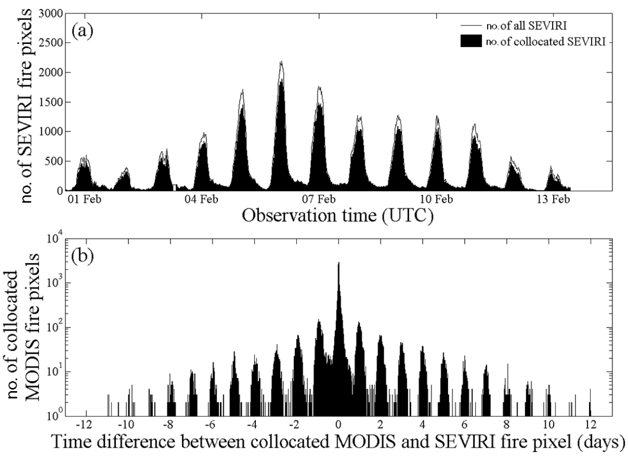


**Figure 20.** Results of the temporal analysis performed using the collocated SEVIRI and MODIS active fire pixels detected in central Africa in Fig. 19. **(a)** Total number of active fire pixels detected by the FTA algorithm in each SEVIRI time slot and the number of those that were within 4 km of a MODIS active fire pixel detected at any time during the study period. **(b)** Number of MODIS active fire pixels detected within 4 km of a SEVIRI fire pixel, expressed as a function of the time difference between the MODIS detection and the most contemporaneous SEVIRI active fire detection. Positive time differences represent a SEVIRI fire detection occurring after the MODIS active fire detection. Note the log scale of the $y$ axis in **(b)**.

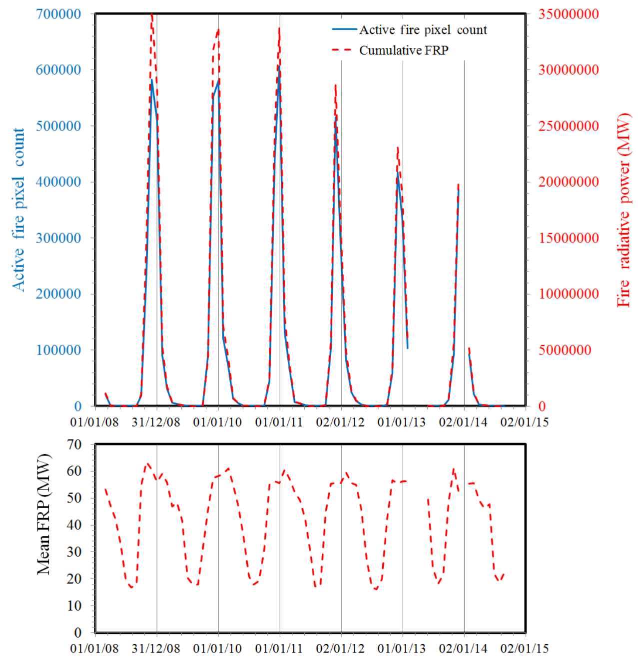


**Figure 21.** Metrics of monthly fire activity (total monthly FRP, monthly active fire pixel count, and the mean per-pixel FRP) for the Central African Republic, as extracted from the 2008–2014 time series of FRP-PIXEL products available from the LSA SAF (http://landsaf.ipma.pt/).

fire pixel located more than 20 km away. The same proximity analysis was repeated to include the full set of SEVIRI active fire pixels detected at all time slots (i.e. all those mapped in Fig. 19c), where 83, 91, and 95 %, respectively, of MODIS fire pixels were found to have a SEVIRI fire pixel within 3, 4, and 5 km, respectively, and fewer than 1 % did not have a SEVIRI counterpart within 20 km. The reverse analysis showed that almost every SEVIRI fire pixel had a MODIS fire pixel within 4 km of it (detected anytime within the two weeks). We conclude that, although the FRP-PIXEL product fails to detect a significant proportion of the MODIS active fire pixels at the time of the MODIS overpass (Fig. 19b) due to their FRP being below the $H_L$ threshold of Fig. 15, the SEVIRI FTA algorithm does detect the vast majority of MODIS-detected fires at some earlier or later stage of their life cycle (Fig. 19c).

Figure 20 indicates the temporal cycle of SEVIRI active fire detections over the region shown in Fig. 19 and the time

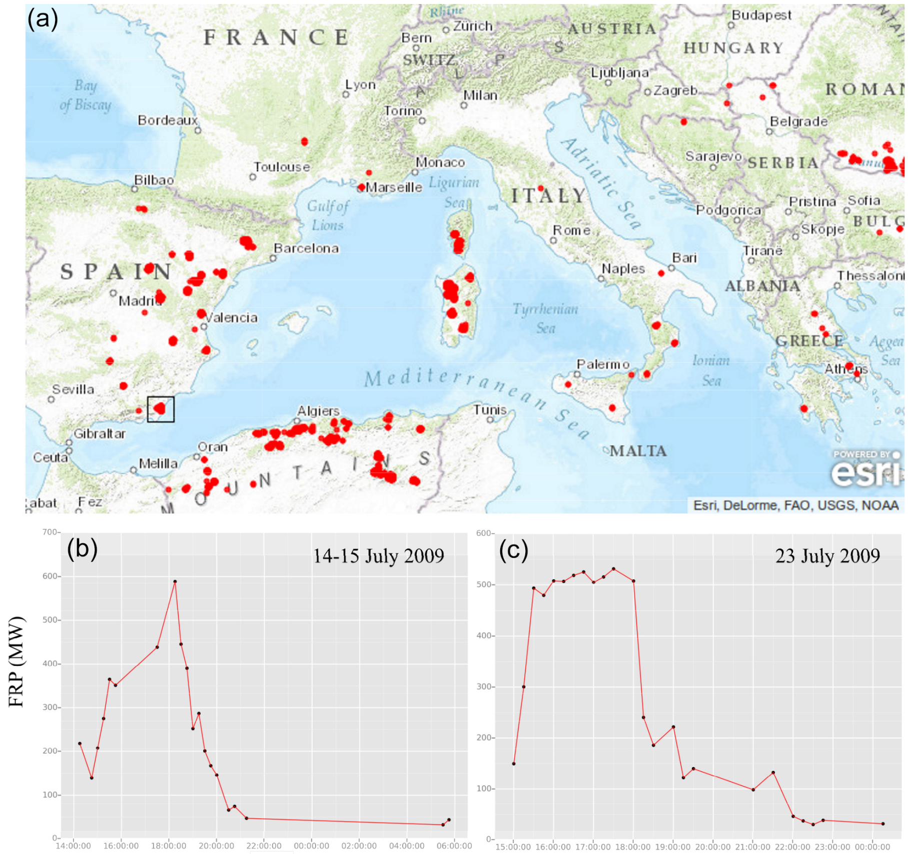


**Figure 22.** High FRP active fire detections made across parts of Europe and North Africa (4.0° E–35.0° W, 25.0–46.0° N) in July 2009 and stored in the SEVIRI FRP-PIXEL product. **(a)** The locations of active fire pixels with FRP $\geq$ 200 MW, with the location of the wildfire close to the Sierra Cabrera in Spain (37.15° N, 1.92° W), are outlined; their FRP time series are shown in **(b)** and **(c)**.

difference within which the matching SEVIRI and MODIS detections of the same fire generally occur (with the matched detections taken as the SEVIRI detection with the minimum time difference to the MODIS detection and located within 4 km of it). Overall, 70, 79, and 84 % of the collocated MODIS fire pixels were detected by SEVIRI within 12, 24, and 36 h, respectively, of the best-matched MODIS observation, with the SEVIRI detection more commonly being after the MODIS detection but quite often occurring before. The 15 min repeat cycle of SEVIRI is well suited for capturing temporal fluctuations in fire behaviour (Roberts et al., 2009a) and is able to capitalize on those opportune moments when a fire does become detectable, notwithstanding the relatively coarse pixel sizes available from geostationary orbit. Figure 21 shows a 6-year time series over the same area with clear cyclic patterns and extremely low FRP pixels dominating outside of the main periods of fire activity. Biomass burning is spatially extensively in the CAR (Fig. 19; Eva and Lambin, 1998; Bucini and Lambin, 2002; Freeborn et al., 2014a, c), and Fig. 21 shows similar patterns in active fire pixel count and total FRP and with some suggestion of a generally decreasing trend in fire activity in recent years (as already noted by Freeborn et al., 2014c, using MODIS).

In terms of the FRP-PIXEL product's ability to provide information relevant to individual large fire events, Fig. 22 shows an example of high FRP ($\geq$ 200 MW pixel$^{-1}$) wildfires detected across the Mediterranean in July 2009 (Pausas and Fernández-Muñoz, 2012). Selecting the single fire pixel that corresponds to the intense wildfire that burned close to Sierra Cabrera (SE Spain), the time series shows that on 14 July this fire expanded and was burning fuel at a rate of 221 kg s$^{-1}$ (calculated using the conversion factor of Wooster et al., 2005) before dying out on 15 July, matching well with news reports of the time (http://en.wikipedia.org/wiki/2009_Mediterranean_wildfires). The same reports indicate that on 23 July the fire flared again, and this second event is also observed in the FRP-PIXEL product time series with the FRP reaching similar heights as seen in the initial blaze (Fig. 21c). FRE-estimated total fuel consumption is estimated to have been in excess of 11 000 t.

## 8 Summary and conclusion

Satellite-based estimates of FRP, including from geostationary satellites, are increasingly used to support regional and global biomass burning emissions calculations (Remy and Kaiser, 2014; Roberts et al., 2011; Vermote et al., 2009; Zhang et al., 2012; Turquety et al., 2014; Baldassarre et al., 2015). We have provided a detailed description of the algorithms and information content of the operational SEVIRI FRP products available from the EUMETSAT LSA SAF, both the FRP-PIXEL product (3 km every 15 min), and the spatio-temporal summary (5°, hourly) FRP-GRID product that includes bias adjustments for cloud cover and SEVIRI's inability to detect the lowest FRP fire pixels. Further information on data formats and content are included in the Supplement.

Using the operational, geostationary FTA algorithm described herein, SEVIRI detects active fire pixels with an FRP down to around 20 MW but those with a FRP $< \sim 30$–40 MW are typically undercounted, hence the requirement for the bias-adjustment factors included in the FRP-GRID product. Using scene simulations and analysis of Meteosat-8 special operations data we demonstrate that certain data pre-processing procedures applied onboard the MSG satellites or in the EUMETSAT IMPF, may not be the optimal for the active fire application. Standard cloud masking procedures also need to be optimized, since they can otherwise mask smoke, or even active fires, as cloud. We recommend consideration of these issues when designing the pre-processing and cloud masking chains to be used with Meteosat Third Generation (MTG), whose sensor has a dedicated low-gain MWIR channel to support active fire applications (Just et al., 2014). Comparisons to the WF-ABBA SEVIRI product indicates strong performance of the FTA algorithm, which detects substantially more active fire pixels, both in any particular SEVIRI time slot and over the full diurnal cycle. The LSA SAF FRP products are therefore well suited to prescribing the typical diurnal cycle of biomass burning regions (Turquety et al., 2014; Andela et al., 2015) and for estimating high temporal resolution wildfire smoke emissions for atmospheric modelling (Baldassarre et al., 2015; Roberts et al., 2015).

**The Supplement related to this article is available online at doi:10.5194/acp-15-13217-2015-supplement.**

*Acknowledgements.* Thanks to G. Fowler and other EUMETSAT staff who contributed to discussions and to our ability to conduct the Meteosat-8 special operations. We also thank Isabel Trigo and all LSA SAF staff for their continued support and dedication. We acknowledge the team that provide the WF-ABBA products, which were developed at the Cooperative Institute for Meteorological Satellite Studies (CIMSS) within the Space Science and Engineering Center (SSEC) at the University of Wisconsin (UW-Madison) as a collaborative effort between NOAA/NESDIS/STAR and UW-CIMSS personnel. Funding for this work came from the UK NERC National Centre for Earth Observation (NCEO), from the LSA SAF project, and from EUMETSAT. MODIS data were courtesy of NASA and SEVIRI data courtesy of EUMETSAT.

Edited by: V.-H. Peuch

## References

Aminou, D. M. A.: MSG's SEVIRI instrument, ESA Bull.-Eur. Space, 111, 15–17, 2002.

Aminou, D. M. A., Jacquet, B., and Pasternak, F.: Characteristics of the Meteosat second generation (MSG) radiometer/imager: SEVIRI, Sensors, Systems, and Next-Generation Satellites, 3221, 19–31, 1997.

Andela, N., Kaiser, J. W., van der Werf, G. R., and Wooster, M. J.: New fire diurnal cycle characterizations to improve fire radiative energy assessments made from MODIS observations, Atmos. Chem. Phys., 15, 8831–8846, doi:10.5194/acp-15-8831-2015, 2015.

Andreae, M. O.: Biomass Burning – Its History, Use, and Distribution and Its Impact on Environmental-Quality and Global Climate, Global Biomass Burning, 3–21, 1991.

Baldassarre, G., Pozzoli, L., Schmidt, C. C., Unal, A., Kindap, T., Menzel, W. P., Whitburn, S., Coheur, P.-F., Kavgaci, A., and Kaiser, J. W.: Using SEVIRI fire observations to drive smoke plumes in the CMAQ air quality model: the case of Antalya in 2008, Atmos. Chem. Phys. Discuss., 15, 1–46, doi:10.5194/acpd-15-1-2015, 2015.

Barnie, T. and Oppenheimer, C.: Extracting High Temperature Event radiance from satellite images and correcting for saturation using Independent Component Analysis, Remote Sens. Environ., 158, 56–68, doi:10.1016/j.rse.2014.10.023, 2015.

Berk, A., Anderson, G. P., Acharya, P. K., Bernstein, L. S., Muratov, L., Lee, J., Fox, M., Adler-Golden, S. M., Chetwynd, J. H., Hoke, M. L., Lockwood, R. B., Gardner, J. A., Cooley, T. W., Borel, C. C., and Lewis, P. E.: MODTRAN (TM) 5, a reformulated atmospheric band model with auxiliary species and practical multiple scattering options: update, P. Soc. Photo.-Opt. Ins., 5806, 662–667, 2005.

Bucini, G. and Lambin, E. F.: Fire impacts on vegetation in Central Africa: a remote-sensing-based statistical analysis, Appl. Geogr., 22, 27–48, 2002.

Calle, A., Casanova, J. L., and Romo, A.: Fire detection and monitoring using MSG Spinning Enhanced Visible and Infrared Imager (SEVIRI) data, J. Geophys. Res.-Biogeo., 111, G04S06, doi:10.1029/2005JG000116, 2006.

Calle, A., Casanova, J. L., and Gonzalez-Alonso, F.: Impact of point spread function of MSG-SEVIRI on active fire detection, Int. J. Remote Sens., 30, 4567–4579, 2009.

Calle, A., Sanz, J., and Casanova, J. L.: Remote sensing for environmental monitoring: forest fire monitoring in real time, in: Water Security in the Mediterranean Region, Springer, Netherlands, 47–64, 2011.

Carvalheiro, L. C., Bernardo, S. O., Orgaz, M. D. M., and Yamazaki, Y.: Forest Fires Mapping and Monitoring of current and past forest fire activity from Meteosat Second Generation data, Environ. Modell. Softw., 25, 1909–1914, 2010.

Clerbaux, C., Boynard, A., Clarisse, L., George, M., Hadji-Lazaro, J., Herbin, H., Hurtmans, D., Pommier, M., Razavi, A., Turquety, S., Wespes, C., and Coheur, P.-F.: Monitoring of atmospheric composition using the thermal infrared IASI/MetOp sounder, Atmos. Chem. Phys., 9, 6041–6054, doi:10.5194/acp-9-6041-2009, 2009.

DaCamara, C. C.: The Land Surface Analysis SAF: one year of pre-operational activity, in: The 2006 EUMETSAT Meteorological Satellite Conference, 48 pp., 2006.

Deneke, H. M. and Roebeling, R. A.: Downscaling of METEOSAT SEVIRI 0.6 and 0.8 μm channel radiances utilizing the high-resolution visible channel, Atmos. Chem. Phys., 10, 9761–9772, doi:10.5194/acp-10-9761-2010, 2010.

Derrien, M. and Le Gleau, H.: Msg/Seviri cloud mask and type from safnwc, Int. J. Remote Sens., 26, 4707–4732, 2005.

Dlamini, W. M.: Characterization of the July 2007 Swaziland fire disaster using satellite remote sensing and GIS, Appl. Geogr., 29, 299–307, 2009.

Eva, H. and Lambin, E. F.: Burnt area mapping in Central Africa using ATSR data, Int. J. Remote Sens., 19, 3473–3497, 1998.

Freeborn, P. H., Wooster, M. J., Hao, W. M., Ryan, C. A., Nordgren, B. L., Baker, S. P., and Ichoku, C.: Relationships between energy release, fuel mass loss, and trace gas and aerosol emissions during laboratory biomass fires, J. Geophys. Res.-Atmos., 113, D01301, doi:10.1029/2007JD008679, 2008.

Freeborn, P. H., Wooster, M. J., Roberts, G., Malamud, B. D., and Xu, W. D.: Development of a virtual active fire product for Africa through a synthesis of geostationary and polar orbiting satellite data, Remote Sens. Environ., 113, 1700–1711, 2009.

Freeborn, P. H., Wooster, M. J., and Roberts, G.: Addressing the spatiotemporal sampling design of MODIS to provide estimates of the fire radiative energy emitted from Africa, Remote Sens. Environ., 115, 475–489, 2011.

Freeborn, P. H., Wooster, M. J., Roberts, G., and Xu, W. D.:Evaluating the SEVIRI fire thermal anomaly detection algorithm across the Central African Republic using the MODIS Active Fire product, Remote Sens., 6, 1890–1917, 2014a.

Freeborn, P. H., Wooster, M. J., Roy, D. P., and Cochrane, M. A.: Quantification of MODIS fire radiative power (FRP) measurement uncertainty for use in satellite-based active fire characterization and biomass burning estimation, Geophys. Res. Lett., 41, 1988–1994, 2014b.

Freeborn, P. H., Cochrane, M. A., and Wooster, M. J.: A decade long, multi-scale map comparison of fire regime parameters derived from three publically available satellite-based fire products: a case study in the Central African Republic, Remote Sens., 6, 4061–4089, 2014c.

Giglio, L., Descloitres, J., Justice, C. O., and Kaufman, Y. J.: An enhanced contextual fire detection algorithm for MODIS, Remote Sens. Environ., 87, 273–282, 2003.

Giglio, L., Csiszar, I., and Justic, C. O.: Global distribution and seasonality of active fires as observed with the Terra and Aqua Moderate Resolution Imaging Spectroradiometer (MODIS) sensors, J. Geophys. Res.-Biogeo., 111, G02016, doi:10.1029/2005JG000142, 2006.

Gonzalo, J., Martín-de-Mercado, G., and Valcarce, F.: Space technology for disaster monitoring, mitigation and damage assessment, in: Space Technologies for the Benefit of Human Society and Earth, Springer, the Netherlands, 305–330, 2009.

Govaerts, Y.: RTMOM V0 B.10 Evaluation Report, report EUM/MET/DOC/06/0502, EUMETSAT, 29 pp., 2006.

Hewison, T. J. and Muller, J.: Ice contamination of Meteosat/SEVIRI implied by intercalibration against Metop/IASI, IEEE T. Geosci. Remote, 51, 1182–1186, 2013.

Hollingsworth, A., Engelen, R. J., Textor, C., Benedetti, A., Boucher, O., Chevallier, F., Dethof, A., Elbern, H., Eskes, H., Flemming, J., Granier, C., Kaiser, J. W., Morcrette, J. J., Rayner, P., Peuch, V. H., Rouil, L., Schultz, M. G., Simmons, A. J., and Consortium, G.: Toward a monitoring and forecasting system for atmospheric composition: the GEMS project, B. Am. Meteorol. Soc., 89, 1147–1164, 2008.

Just, D.: SEVIRI instrument Level 1.5 data. Proceedings of the First MSG RAO Workshop, 17–19 May 2000: Bologna, Italy, Edited by R. A. Harris, European Space Agency ESASP-452, 29–37, 2000.

Just, D., Gutiérrez, R., Roveda, F., and Steenbergen, T.: Meteosat third generation imager: simulation of the flexible combined imager instrument chain, P. Soc. Photo.-Opt. Ins., 9241, doi:10.1117/12.2066872, 2014.

Kaiser, J. W., Heil, A., Andreae, M. O., Benedetti, A., Chubarova, N., Jones, L., Morcrette, J.-J., Razinger, M., Schultz, M. G., Suttie, M., and van der Werf, G. R.: Biomass burning emissions estimated with a global fire assimilation system based on observed fire radiative power, Biogeosciences, 9, 527–554, doi:10.5194/bg-9-527-2012, 2012.

Kremens, R. L., Dickinson, M. B., and Bova, A. S.: Radiant flux density, energy density and fuel consumption in mixed-oak forest surface fires, Int. J. Wildland Fire, 21, 722–730, 2012.

Libonati, R., DaCamara, C. C., Pereira, J. M. C., and Peres, L. F.: Retrieving middle-infrared reflectance for burned area mapping in tropical environments using MODIS, Remote Sens. Environ., 114, 831–843, 2010.

Liu, Y., Kahn, R. A., Chaloulakou, A., and Koutrakis, P.: Analysis of the impact of the forest fires in August 2007 on air quality of Athens using multi-sensor aerosol remote sensing data, meteorology and surface observations, Atmos. Environ., 43, 3310–3318, 2009.

Mayaux, P., Bartholome, E., Fritz, S., and Belward, A.: A new land-cover map of Africa for the year 2000, J. Biogeogr., 31, 861–877, 2004.

MeteoFrance: Algorithm Theoretical Basis Document for Cloud Products, 2010.

Murphy, D.: EUMETSAT geostationary meteorological satellite programs, in: Handbook of Satellite Applications, Springer, New York, 991–1019, 2013.

Pausas, J. G. and Fernández-Muñoz, S.: Fire regime changes in the Western Mediterranean Basin: from fuel-limited to drought-driven fire regime, Climatic Change, 110, 215–226, 2012.

Pereira, G., Shimabukuro, Y. E., Moraes, E. C., Freitas, S. R., Cardozo, F. S., and Longo, K. M.: Monitoring the transport of biomass burning emission in South America, Atmos. Pollution Res., 2, 247–254, 2011.

Prins, E. M., Feltz, J. M., Menzel, W. P., and Ward, D. E.: An overview of GOES-8 diurnal fire and smoke results for SCAR-B and 1995 fire season in South America, J. Geophys. Res.-Atmos., 103, 31821–31835, 1998.

Qin, Z. and Karnieli, A.: Progress in the remote sensing of land surface temperature and ground emissivity using NOAA-AVHRR data, Int. J. Remote Sens., 20, 2367–2393, 1999.

Reid, J. S., Hyer, E. J., Prins, E. M., Westphal, D. L., Zhang, J. L., Wang, J., Christopher, S. A., Curtis, C. A., Schmidt, C. C., Eleuterio, D. P., Richardson, K. A., and Hoffman, J. P.: Global monitoring and forecasting of biomass-burning smoke: description of and lessons from the Fire Locating and Modeling of Burning Emissions (FLAMBE) program, IEEE J. Sel. Top. Appl., 2, 144–162, 2009.

Remy, S. and Kaiser, J. W.: Daily global fire radiative power fields estimation from one or two MODIS instruments, Atmos. Chem. Phys., 14, 13377–13390, doi:10.5194/acp-14-13377-2014, 2014.

Roberts, G. and Wooster, M. J.: Fire detection and fire characterization over Africa using Meteosat SEVIRI, IEEE T. Geosci. Remote, 46, 1200–1218, 2008.

Roberts, G. and Wooster, M.: Development of a multi-temporal Kalman filter approach to geostationary active fire detection and fire radiative power (FRP) estimation, Remote Sens. Environ., 152, 392–412, 2014.

Roberts, G., Wooster, M. J., Perry, G. L. W., Drake, N., Rebelo, L. M., and Dipotso, F.: Retrieval of biomass combustion rates and totals from fire radiative power observations: application to southern Africa using geostationary SEVIRI imagery. J. Geophys. Res., 110, D21111, doi:10.1029/2005JD006018, 2005.

Roberts, G., Wooster, M. J., and Lagoudakis, E.: Annual and diurnal african biomass burning temporal dynamics, Biogeosciences, 6, 849–866, doi:10.5194/bg-6-849-2009, 2009a.

Roberts, G., Wooster, M. J., Lagoudakis, E., Freeborn, P., and Xu, W.: Continental Africa Biomass Burning Temporal Dynamics derived from MSG SEVIRI, Int. Geosci. Remote Se., 1–5, 1458–1461, 2009b.

Roberts, G., Wooster, M., Freeborn, P. H., and Xu, W.: Integration of geostationary FRP and polar-orbiter burned area datasets for an enhanced biomass burning inventory, Remote Sens. Environ., 115, 2047–2061, 2011.

Roberts, G., Wooster, M. J., Xu, W., Freeborn, P. H., Morcrette, J.-J., Jones, L., Benedetti, A., Jiangping, H., Fisher, D., and Kaiser, J. W.: LSA SAF Meteosat FRP products – Part 2: Evaluation and demonstration for use in the Copernicus Atmosphere Monitoring Service (CAMS), Atmos. Chem. Phys., 15, 13241–13267, doi:10.5194/acp-15-13241-2015, 2015.

Ross, A. N., Wooster, M. J., Boesch, H., and Parker, R.: First satellite measurements of carbon dioxide and methane emission ratios in wildfire plumes, Geophys. Res. Lett., 40, 4098–4102, 2013.

Schmetz, J., Pili, P., Tjemkes, S., Just, D., Kerkmann, J., Rota, S., and Ratier, A.: An introduction to Meteosat Second Generation (MSG), B. Am. Meteorol. Soc., 83, 977–992, 2002.

Schroeder, W., Oliva, P., Giglio, L., and Csiszar, I. A.: The New VIIRS 375,m active fire detection data product: algorithm description and initial assessment, Remote Sens. Environ., 143, 85–96, 2014.

Sofiev, M., Vankevich, R., Lotjonen, M., Prank, M., Petukhov, V., Ermakova, T., Koskinen, J., and Kukkonen, J.: An operational system for the assimilation of the satellite information on wildland fires for the needs of air quality modelling and forecasting, Atmos. Chem. Phys., 9, 6833–6847, doi:10.5194/acp-9-6833-2009, 2009.

Trigo, I. F., Dacamara, C. C., Viterbo, P., Roujean, J. L., Olesen, F., Barroso, C., Camacho-de-Coca, F., Carrer, D., Freitas, S.C., Garcia-Haro, J., Geiger, B., Gellens-Meulenberghs, F., Ghilain, N., Melia, J., Pessanha, L., Siljamo, N., and Arboleda, A.: The satellite application facility for land surface analysis, Int. J. Remote Sens., 32, 2725–2744, 2011.

Turquety, S., Menut, L., Bessagnet, B., Anav, A., Viovy, N., Maignan, F., and Wooster, M.: APIFLAME v1.0: high-resolution fire emission model and application to the Euro-Mediterranean region, Geosci. Model Dev., 7, 587–612, doi:10.5194/gmd-7-587-2014, 2014.

van der Werf, G. R., Randerson, J. T., Collatz, G. J., and Giglio, L.: Carbon emissions from fires in tropical and subtropical ecosystems, Glob. Change Biol., 9, 547–562, 2003.

van der Werf, G. R., Randerson, J. T., Giglio, L., Collatz, G. J., Kasibhatla, P. S., and Arellano Jr., A. F.: Interannual variability in global biomass burning emissions from 1997 to 2004, Atmos. Chem. Phys., 6, 3423–3441, doi:10.5194/acp-6-3423-2006, 2006.

Vermote, E., Ellicott, E., Dubovik, O., Lapyonok, T., Chin, M., Giglio, L., and Roberts, G. J.: An approach to estimate global biomass burning emissions of organic and black carbon from MODIS fire radiative power, J. Geophys. Res.-Atmos., 114, D18205, doi:10.1029/2008JD011188, 2009.

Wooster, M. J., Zhukov, B., and Oertel, D.: Fire radiative energy for quantitative study of biomass burning: derivation from the BIRD experimental satellite and comparison to MODIS fire products, Remote Sens. Environ., 86, 83–107, 2003.

Wooster, M. J., Roberts, G., Perry, G. L. W., and Kaufman, Y. J.: Retrieval of biomass combustion rates and totals from fire radiative power observations: FRP derivation and calibration relationships between biomass consumption and fire radiative energy release, J. Geophys. Res.-Atmos., 110, D24311, doi:10.1029/2005JD006318, 2005.

Wooster, M. J., Xu, W., and Nightingale, T.: Sentinel-3 active fire detection and FRP product: pre-launch algorithm development and performance evaluation using MODIS and ASTER datasets, Remote Sens. Environ., 120, 236–254, 2012.

Wooster, M. J., Roberts, G., Smith, A. M., Johnston, J., Freeborn, P., Amici, S., and Hudak, A. T.: Thermal remote sensing of active vegetation fires and biomass burning events, in: Thermal Infrared Remote Sensing, Springer, Netherlands, 347–390, 2013.

Xu, W., Wooster, M. J., Roberts, G., and Freeborn, P.: New GOES imager algorithms for cloud and active fire detection and fire radiative power assessment across North, South and Central America, Remote Sens. Environ., 114, 1876–1895, 2010.

Zhang, X. Y., Kondragunta, S., Ram, J., Schmidt, C., and Huang, H. C.: Near-real-time global biomass burning emissions product from geostationary satellite constellation, J. Geophys. Res.-Atmos., 117, D14201, doi:10.1029/2012JD017459, 2012.

Zhukov, B., Lorenz, E., Oertel, D., Wooster, M., and Roberts, G.: Spaceborne detection and characterization of fires during the bi-spectral infrared detection (BIRD) experimental small satellite mission (2001–2004), Remote Sens. Environ., 100, 29–51, 2006.